

The Mechanisms of Non-Photochemical Laser-Induced Nucleation

Theory and Experiment

T.P. van Waas



The Mechanisms of Non-Photochemical Laser-Induced Nucleation

Theory and Experiment

by

T.P. van Waas

In partial fulfillment of the degree of
Bachelor of Science Molecular Science & Technology
at Delft University of Technology,
to be defended publicly on Wednesday August 21, 2019 at 11:00 AM.

Student number:	4515560	
Project duration:	April 22, 2019 – August 21, 2019	
Under guidance and supervision of:	Dr. D. Irimia, Dr. H.B. Eral,	TU Delft, daily supervisor TU Delft, supervisor
Thesis committee:	Dr. H.B. Eral, Prof. A. van der Heijden, Dr. V. van Steijn,	TU Delft, supervisor TU Delft TU Delft

This thesis is confidential and cannot be made public until August 21, 2019.

An electronic version of this thesis is available at <http://repository.tudelft.nl/>.

Cover image: Ammonium chloride crystals in an electrolyte solution pulsed by a 532 nm laser, growing into an octahedral structure.

Acknowledgements

I am indebted to many researchers and co-workers from various departments and universities who have assisted me over the course of my research project. Firstly, I would like to thank my experimental supervisor, Dr. Daniel Irimia. We will be the only ones to know the difficulty of problems that we have faced during the creation of the experimental setup. It was also incredibly satisfying to overcome these issues collaboratively, relying on our knowledge and perseverance. Secondly, I am thankful for Burak Eral for introducing me to many interesting people, emphasising that science is a collaborative undertaking. It was always my desire to find a bachelor project where I could test my skills in chemistry and physics together, and during the project I was certainly able to challenge myself on both of the subjects sufficiently. Furthermore, I appreciate the people who have taught me the details of working in the laboratory, especially Fandy and Alex. I would also like to thank members of the NPLIN team for all the lively discussions, including Herman, Antoine, Alberto and Izak. I will certainly miss the opportunity for discussing scientific subjects with so many knowledgeable and engaged people every week. I would also like to acknowledge Dr. Remco Hartkamp, Dr. Jan Groenewold and Dr. Andrew Alexander for sharing their thoughts on various research phenomena. I am thankful for Aditya, Iman and Niels for many insightful discussions on science and academia, showing me that it is really worthwhile to deeply engage with a scientific topic for a longer period of time. And lastly I would like to thank Fleur, for always providing the atmosphere I need for getting my thoughts off of scientific topics at the end of the day.

Abstract

Non-photochemical laser-induced nucleation (NPLIN) is a crystallisation method in which a highly structured phase is formed out of solution by exposure to a laser beam. NPLIN offers unprecedented spatiotemporal control and characterisation of nucleation. NPLIN is energy efficient compared to conventional crystallisation methods and can be implemented in continuous microfluidic reactors, enabling sustainable operation. However, its working principles are not yet fully understood. This study contains an evaluation of four proposed mechanisms and a description of an experimental setup involving an ultrahigh speed camera. Two mechanisms describe interaction of molecular polarisation with the electric field, either isotropically known as *dielectric polarisation* (DP), or anisotropically via the *optical Kerr effect* (OKE). The other two mechanisms involve cavitation bubble formation by nanoparticle heating through light absorption. This work contains a refined description of this so-called *cavity-induced nucleation* where its consequences are distinguished into two mechanisms, either based on *concentration enhancement* (CICEN) or due to *pressure enhancement* (CIPEN). Novel theoretical calculations in conjunction with experimental data suggest that NPLIN phenomena are based on DP or CICEN, potentially operating in concert. It is conjectured that the influence of DP and CICEN can be quantified further by development of a topological description of DP, simulations of CICEN and relating nucleation probabilities to the metastable zone width of various solutes. The calculations suggest that OKE and CIPEN have little significance because involved energies are several orders of magnitude below $k_B T$. The proposed setup allows for observing the NPLIN phenomena and establishing dependence on cavitation bubbles, providing empirical validation. Solutions to experimental problems are provided, including reduction of sample fluid evaporation, aligning the nucleation site with the region of interest of the camera and removing image noise.

Contents

1	Introduction	1
1.1	Relevance	1
1.2	Classical and Two-step Nucleation Theories	1
1.3	Non-Photochemical Laser Induced Nucleation	3
1.4	Thesis Objective	4
2	Theory	5
2.1	Mechanism I: Dielectric Polarisation	5
2.1.1	Minimum Pulse Duration for Dielectric Polarisation	7
2.2	Mechanism II: Optical Kerr Effect	8
2.3	Nanoparticle Heating	9
2.4	Mechanism III: Cavity-Induced Concentration Enhanced Nucleation	10
2.5	Mechanism IV: Cavity-Induced Pressure Enhanced Nucleation	11
2.5.1	Pressure Contributions to the Chemical Potential	12
3	Experimental Methods	13
3.1	Software	13
3.2	The Laser Setup	13
3.3	Imaging settings	14
3.4	Post-processing	15
3.5	Sample Preparation	16
3.6	Metastable Zone Width Determination	17
4	Results & Discussion	19
4.1	Laser Intensity Results	19
4.2	Image Post-Processing	20
4.3	Metastable Zone Width Results	22
5	Conclusions & Recommendations	23
5.1	Conclusions	23
5.2	Recommendations	24
	Bibliography	25
A	Uncertainties	31

Introduction

1.1. Relevance

Currently, fine chemical and pharmaceutical sectors are causing the largest waste production per mass of product in chemical engineering, with ratios up to 10-100 kg waste per kg product [1]. In addition, production and work-up methods used in these sectors are energy-intensive. Crystallisation is the formation of a solid phase with a highly organised structure from another phase [2]. It is a widely used production method in chemical industries, where the crystallisation is often achieved by evaporation of the solvent or by significant cooling of the solution. In Europe, roughly 1% of the energy consumed by industries is renewable [3], while industries are accountable for half of the energy consumed worldwide [4]. These high waste productions and the non-renewable energy consumption emphasise a high demand for innovative, low-waste and energy friendly crystallisation methods in industry.

The proposed method in this paper is based on NPLIN: non-photochemical laser-induced nucleation, which is readily being applied to salts, small organic compounds and proteins, as shown in recent studies [5–7]. NPLIN has shown an increase in crystallisation rates of up to $\mathcal{O}(10^6)$.

NPLIN is the process where solid nuclei or vapour bubbles are formed from a distinct phase using a laser. By quantisation of electron excitation, Photochemical laser-induced nucleation (PLIN) is often strongly dependent on the wavelength and weakly dependent on the intensity [8]. By contrast, NPLIN is marginally dependent on the wavelength and strongly dependent on the intensity, suggesting that it is distinct from PLIN [9].

1.2. Classical and Two-step Nucleation Theories

Crystallisation is initiated by nucleation, which is the formation of a distinct thermodynamic phase, often from a solution [10]. Nucleation is followed by crystal growth. Formation of the first nuclei is called primary nucleation, whereas occurrence of additional nuclei, e.g. by fracturing of the initial nucleus, is called secondary nucleation. Primary nucleation is divided in homogeneous nucleation, i.e. nucleation where the solution is the only relevant initial phase, and heterogeneous nucleation, where a second phase facilitates the formation of nuclei. In classical nucleation theory (CNT), homogeneous nucleation occurs when the change in Gibbs energy ΔG at isobaric conditions is negative. The free energy change by formation of a solid phase from a liquid phase is given by [11]:

$$\Delta G = s\sigma + V\rho\Delta\mu, \quad (1.1)$$

where s is the interfacial area, γ is the surface tension, V is the volume of the crystal, ρ is the volumetric particle density in the crystal phase, and the driving term $\Delta\mu = \mu_s - \mu_l$ is the change in chemical potential from the liquid phase of chemical potential μ_l towards the solid phase of chemical potential μ_s . Often, $s\sigma$ is denoted as the surface Gibbs energy change, whereas $Vn\Delta\mu$ is denoted as the volumetric Gibbs energy change. At isochoric conditions, nucleation can occur if the Helmholtz energy ΔA is negative. Nucleation rates are often exponentially dependent on the ratio of $\Delta G/(k_B T)$ where k_B is the Boltzmann constant and T is the temperature. A first order evaluation of the influence of any theory can be provided by a comparison of energy changes to the microscopic energy of particles, $k_B T = 25.6$ meV at $T = 298$ K. If a mechanism involves

energies that are lower by several orders of magnitude, the mechanism is unlikely to have any significant consequences [12].

Assuming a radially symmetric crystal, Equation 1.1 becomes

$$\Delta G = 4\pi r^2 \sigma + \frac{4}{3}\pi r^3 \rho \Delta\mu, \quad (1.2)$$

where r is the crystal radius. In CNT, it is often assumed that the solution contains a time independent size distribution of precritical clusters [13]. Equation 1.2 ensures that nuclei are formed if the critical radius r_c satisfies:

$$r_c = -\frac{2\sigma}{\rho\Delta\mu}. \quad (1.3)$$

where the chemical potential in the liquid phase is given as $\mu_l = \mu_l^\circ + k_B T \ln(S)$ [14], where

$$S_T = \frac{c(T)}{c_s(T)} \quad (1.4)$$

is the selected definition for this paper in terms of the concentration $c(T)$ and the concentration at saturation $c_s(T)$, where T in S_T denotes the saturation temperature in °C. Under the assumption that terms such as the activity coefficient γ do not significantly influence μ_l° , the chemical potential difference reduces to

$$\Delta\mu \approx -k_B T \ln(S). \quad (1.5)$$

Differential changes to the chemical potential through a temperature change ΔT and a pressure change ΔP follow the Gibbs-Duhem equation [15]:

$$d\mu = -\Delta V dP + \Delta S dT, \quad (1.6)$$

where ΔV and ΔS are the volume and entropy changes of crystallisation, respectively. As generally $\Delta V > 0$, ΔP will correlate positively with nucleation rates, whereas ΔT will correlate negatively with nucleation rates given $\Delta S < 0$.

The above derivation allows for an explanation of the concentration-temperature phase diagram of solutes, as shown in Figure 1.1.

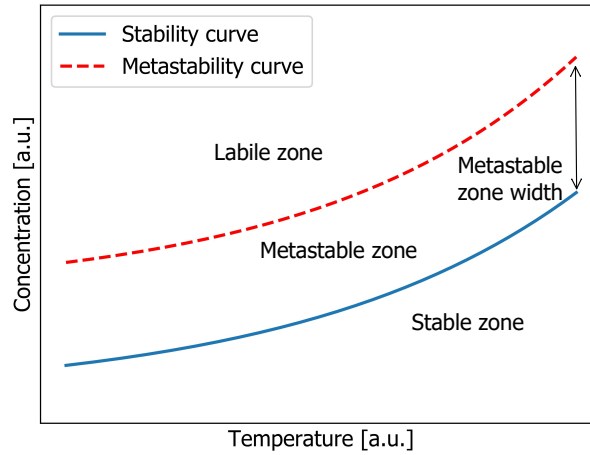


Figure 1.1: A concentration-temperature phase diagram for a typical solute. In the labile zone, both spontaneous nucleation and crystal growth can occur. In the metastable zone, crystal growth occurs for existing crystals. In the stable zone, neither of the processes occur and crystals will redissolve. The metastable curve is dashed to display its dependence on kinetics.

Here, the metastable zone width (MSZW) is defined as the concentration difference at a particular solution temperature and cooling rate between the stability curve and the metastability curve. For a given temperature at a concentration below c_s , a solution is stable because of a positive $\Delta\mu$ and spontaneous nucleation will not occur. Consequently, the stability curve is thermodynamic, i.e. dynamically invariant. Passing the stability curve, $\Delta\mu$ becomes negative and existing crystals will grow. At sufficiently high concentrations, the Gibbs volumetric energy change ensures that ΔG also becomes negative, leading to spontaneous nucleation.

Moreover, two-step nucleation (TSN) theories propose a transient size distribution of precritical clusters. This could explain why the metastability curve is kinetic: observation of crystals depends on solution conditions such as stirring rates and nucleation induction times [13]. Recently, molecular dynamics (MD) simulations combined with experimental electron tomography point towards the existence of precritical clusters as proposed by TSN [16]. The MSZW will be particularly important for mechanisms that rely on local temperature and concentration changes.

1.3. Non-Photochemical Laser Induced Nucleation

Since the discovery of NPLIN by Garetz *et al.* [17], understanding of NPLIN has increased and nomenclature has been refined. However, the potential mechanisms are still under debate and modification. To understand how the presence of a laser influences terms in Equation 1.1 requires an understanding of how the laser can interact with a solution. Moreover, initial experiments suggested that the laser favoured the growth of specific polymorphs and suggested a direct correlation between the laser polarisation and the crystal orientation [18]. Polymorphs are unique crystalline arrangements of a particular molecular phase. Although polymorphic control could be strongly beneficial to many processes, it is only applied in a small number of crystallisation methods [19]. NPLIN experiments for the nucleation of specific molecules or polymorphs have actively been conducted in recent years [20, 21], although any direct correlation between the laser polarisation and macroscopic orientation of crystals has lost statistical significance due to repeated experiments [22]. *Polarisation switching* was the name given to the notion that the polarisation of light could influence the morphology of the nuclei.

Another promising feature is that it allows for careful study of the nucleation phenomenon itself. Despite its importance, it may be argued that nucleation is still poorly understood, with modern analysis techniques still leading to new discoveries [16]. A focusing beam and intensity threshold could offer unprecedented spatiotemporal control of nucleation phenomena, allowing for imaging and spectroscopic analysis. Consequently, NPLIN may allow for dictating the nucleation and growth phenomena at the molecular level. Recently, it has been shown that NPLIN is observable in microfluidic channels [23], corroborating the notion that NPLIN potentially offers unprecedented control over crystallisation processes.

It is likely that modest intensities will be required for the process of NPLIN. At sufficiently high intensities, an electro field can simply ionise particles in the beam path, known as optical breakdown [24]. What makes NPLIN unique is the unprecedented spatiotemporal and morphological control, which is only expected within a specific experimental intensity range, as displayed in Figure 1.2. Determining the experimental range is a proposed first step for the construction of any experimental setup used for NPLIN experiments.

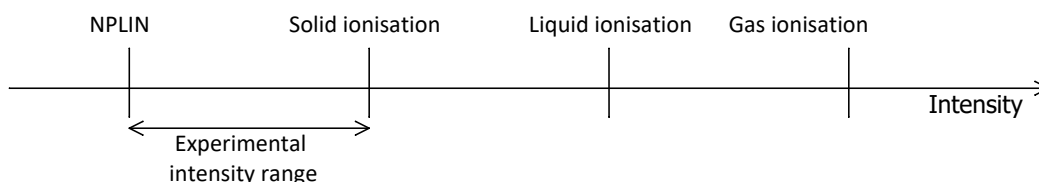


Figure 1.2: The observed thresholds for the effects of NPLIN, and ionisation of solids, liquids and gases, known as optical breakdown. It is suggested that the distinctive characteristics from NPLIN are only expected within the experimental intensity range.

The ways in which the laser beam can interact with the material will now be described. Effectively, a laser pulse or beam consists of electromagnetic waves. Consequently, there are three possible pathways: absorption of electromagnetic energy, phase energy change due to the electric field, and phase energy change due to the magnetic field [25]. Quantum-mechanically, electrons in exposed materials can be excited by absorption of photons, defined as quanta of electromagnetic radiation. Interestingly, these transitions are quantised, i.e. excitation for atoms and small molecules can only occur at particular wavelengths. A size increase in materials often leads to absorption in a broad spectrum due interactions between electron orbitals. Because of the weak independence on the wavelength, it is likely that uptake of electromagnetic energy in simple electrolyte requires larger molecules of particles different from the water and any added solutes. Alternatively, the electric component of the laser beam may change the stability of relevant phases by adding an electric energy term to Equation 1.1 [9]. Recently, a thermodynamic model for electric field induced phase separation driven has been developed [26]. Lastly, the magnetic component of the field may change the stability of relevant phases. However, the magnetic component is often disregarded because most materials are hardly affected

by magnetic fields [27], despite the magnetic component of the field carrying an equal amount of energy as the electric component.

1.4. Thesis Objective

The central objective is to clarify the mechanisms of NPLIN and to devise an experimental procedure which allows for discerning between these mechanisms in a sustainable procedure. Progress for this objective should be achieved along the following lines:

- The different mechanisms behind NPLIN will be thoroughly discussed, along with the development of numerical frameworks which will allow for verification of the theories.
- The relation between the MSZW and NPLIN will be investigated, as some theories depend on a direct relation between the MSZW and observed nucleation rates.
- An experimental procedure will be constructed which allows for imaging of NPLIN phenomena, providing spatiotemporal characterisation of observed events.
- Possible means of reducing involved energy consumption and material usage will be addressed, so that the experiments can be performed in a more sustainable fashion.

2

Theory

In this chapter, the relevant theories of NPLIN will be discussed. The first two methods are related to polarisation of molecules due to the electric field. Nucleation rate increases due to particle migration under the electric field are insignificant laser intensities characteristic for NPLIN experiments [28]. The first mechanism is called *dielectric polarisation* (DP), described in Section 2.1. The second mechanism is the *optical Kerr effect* (OKE) described in Section 2.2. The third mechanism will be denoted as the *cavity-induced concentration enhanced nucleation* (CICEN) and is described in Section 2.4. The fourth mechanism will be denoted as *cavity-induced pressure enhanced nucleation* (CIPEN) and is described in Section 2.5. The first two theories are well-known within the NPLIN debate. The latter two theories may be regarded as refinement or elucidation of existing theories based on the heating of a nanoparticle due to the absorption of electromagnetic energy. Notably, there is no trivial way in which these mechanisms could enhance or inhibit one another. Therefore, observed phenomena may be the consequence of the interplay of a multitude of mechanisms.

2.1. Mechanism I: Dielectric Polarisation

The electric component of the electromagnetic field from the laser beam can interact with any isotropic material through an induction of a transient polarisation, known and is therefore known as *dielectric polarisation* [28]. This effect does not require the electric bodies to have a net non-zero charge or any static polarisation [29] and can therefore be applied to any molecule type. Given a region of volume V containing a dielectric body - such as a crystal - of relative permittivity ϵ_p in a homogeneous dielectric medium - such as a solution - of relative permittivity ϵ_s , it is found that $\Delta\Delta G = \alpha V(\epsilon_s - \epsilon_p)E^2$, which is commonly negative because $\epsilon_p > \epsilon_s$ which originates from the induced electric dipole interaction $-pE$, where p is the dipole moment [7]. Consequently, the average electric field intensity $I = \frac{1}{2}\epsilon_0 c E^2$ contributes to the chemical potential, where $c = 1/\sqrt{\mu\epsilon}$ is the speed of light in the medium of electric permittivity ϵ and magnetic permeability μ , so that for a spherical particle, Equation 1.2 is adjusted to

$$\Delta G(r, I) = 4\pi r^2 \sigma - \frac{4}{3}\pi r^3 (\rho k_B T \ln(S) + \epsilon^* I), \quad (2.1)$$

where ϵ^* is the effective permittivity given as [7]

$$\epsilon^* = \frac{3\epsilon_s(\epsilon_p - \epsilon_s)}{c(\epsilon_p + 2\epsilon_s)}. \quad (2.2)$$

Note again that no contribution is attributed to the magnetic field because of much weaker interactions with nearly all compounds. Consequently, the dielectric polarisation shifts the critical radius towards

$$r_c(I) = \frac{2\sigma}{\rho k_B T \ln(S) + \epsilon^* I}, \quad (2.3)$$

whereas the maximum Gibbs energy for a critical cluster is changed to

$$\Delta G(r_c, I) = \frac{16\pi\sigma^3}{3(\rho k_B T \ln(S) + \epsilon I)}. \quad (2.4)$$

The changes in the critical radius and Gibbs energy are small for nearly any solute [9]. However, it is known from transition state theory that small changes to parameters and energies of phase transitions may invoke large consequences. [30].

The following derivation is taken from Alexander & Camp [9] in order to quantitatively relate mathematical expressions with obtained results. According to TSN, the average number of precritical clusters in a supersaturated solution is given by

$$N_{cluster} = \frac{N_{molecule}}{\langle N \rangle}, \quad (2.5)$$

where $N_{molecule}$ is the number of solute molecules that can be formed from the solution and $\langle N \rangle$ is the average number of molecules in a cluster, which for spherical clusters in a Gibbs ensemble is given by

$$\langle N \rangle = \frac{4\pi\rho\langle r^3 \rangle}{3} = \frac{4\pi}{3} \cdot \frac{\int_0^{r_c(0)} r^3 e^{-\Delta G(r,0)/(k_B T)} \mathbf{d}r}{\int_0^{r_c(0)} e^{-\Delta G(r,0)/(k_B T)} \mathbf{d}r}. \quad (2.6)$$

In Equation 2.6, the mean radius follows from its statistical moment divided by the partition function for normalisation. The number of clusters that will form viable crystals is the number of crystals times the fraction of clusters that are prone to nucleation in the presence of the electric field:

$$N_{crystal} = N_{cluster} \cdot \frac{\int_{r_c(I)}^{r_c(0)} e^{-\Delta G(r,0)/(k_B T)} \mathbf{d}r}{\int_0^{r_c(0)} e^{-\Delta G(r,0)/(k_B T)} \mathbf{d}r}. \quad (2.7)$$

Combining equations 2.6 and 2.7 yields the number of crystals as

$$N_{crystal} = \frac{3N_{molecule}}{4\pi\rho} \cdot \frac{\int_{r_c(I)}^{r_c(0)} e^{-\Delta G(r,0)/(k_B T)} \mathbf{d}r}{\int_0^{r_c(0)} r^3 e^{-\Delta G(r,0)/(k_B T)} \mathbf{d}r}. \quad (2.8)$$

Subsequently, $r_c(0) - r_c(I) \ll r_c(0)$ because the difference in radii is small, so that the integral can be approximated as a difference:

$$\int_{r_c(0)}^{r_c(I)} e^{-\Delta G(r,0)/(k_B T)} \mathbf{d}r \approx e^{-\Delta G_c(r_c,0)/(k_B T)} (r_c(0) - r_c(I)). \quad (2.9)$$

Additionally, under the approximation that $\varepsilon^* I \ll nk_B T \ln(\gamma S)$ for weak electric fields, the radial difference can be approximated as

$$r_c(0) - r_c(I) = \frac{2\sigma\varepsilon^* I}{(\rho k_B T \ln(S))^2}. \quad (2.10)$$

As the probability of nucleation in separate experiments is independent, the probability that no nucleation is a typical experiment is equal to $e^{-N_{crystal}}$ for a Poisson process, where $N_{crystal}$ is the average number of viable crystals under the influence of the laser. The probability of nucleation then becomes

$$p_{nucleation} = 1 - e^{-N_{crystal}}. \quad (2.11)$$

The derivation can be pursued further to determine the probability dependence of nucleation on the intensity. $N_{crystal}$ can be decomposed into its intensity independent part m and the intensity I as $N_{crystal} = mI$, where

$$m = \frac{3N_{molecule}\sigma\varepsilon^*}{2\pi\rho^3 (k_B T \ln(S))^2} \cdot \frac{e^{-\Delta G(r_c,0)/(k_B T)}}{\int_0^{r_c(0)} r^3 e^{-\Delta G(r,0)/(k_B T)} \mathbf{d}r}, \quad (2.12)$$

so that nucleation probabilities can be compared to experimental data. To comply with a potential threshold intensity $I_{threshold}$, Equation 2.11 is often finalised into

$$p_{nucleation} = 1 - e^{-m(I-I_{threshold})}. \quad (2.13)$$

A comparison for KCl was conducted by Alexander & Camp [9], including a description of all of the relevant parameters. The selected intensity was $I = 15 \text{ MW}/(\text{cm})^2$, a typical intensity for NPLIN experiments [6].

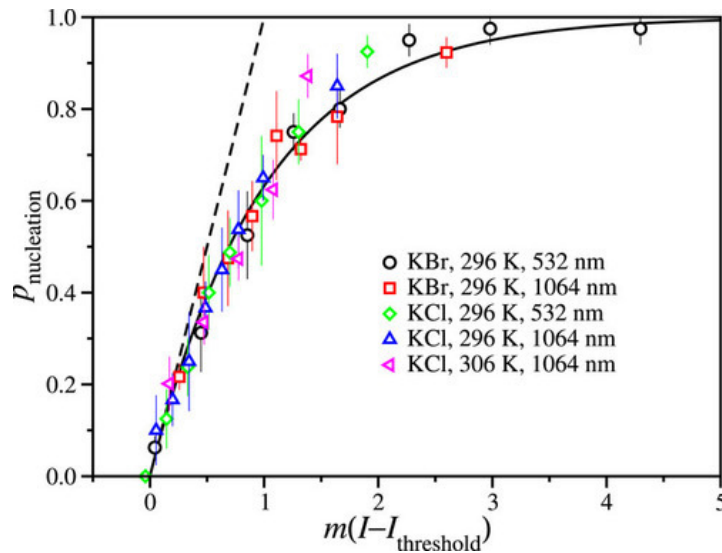


Figure 2.1: Fitting the nucleation probability to the intensity above the threshold intensity $I - I_{threshold}$ for the potassium halides KBr and KCl for wavelengths $\lambda = 532$ nm and $\lambda = 1064$ nm. All experiments were performed at $S_{23} = 1.060$. Image obtained from Alexander & Camp [9].

Notably, σ has been the only fit parameter for the curve fitting in Figure 2.1. Furthermore, it is observed that the threshold intensity varies slightly with the wavelength λ , which is attributed to the absorption coefficient of water [31].

2.1.1. Minimum Pulse Duration for Dielectric Polarisation

The question arises whether DP is able to explain NPLIN for short laser pulses, as induced dipoles may quickly decay in the absence of a pulse. According to the diffusion relation, the maximum displacement for bulk limited particle diffusion is given by [32]:

$$R \leq \sqrt{4D\Delta t}, \quad (2.14)$$

where D is the diffusion coefficient. This equation can be rewritten to obtain the minimum pulse duration for particles to diffuse from the sphere of radius R :

$$\Delta t_p \geq \frac{R^2}{4D}, \quad (2.15)$$

which provides a means for distinguishing between theories which either require structural order to appear within the duration of the pulse such as DP, or allow for clustering in a time period after the laser pulse due to disruption of the system. R can subsequently be obtained from a mass balance for the solute according to:

$$\frac{4}{3}\pi R^3 \rho_s \frac{m_s}{m_{sol}} = \frac{4}{3}\pi r_c^3 \rho_c, \quad (2.16)$$

where ρ_s is the density of the solution, $\frac{m_s}{m_{sol}}$ is the mass fraction of salt in solution and ρ_c is the density of the formed crystal. As an example, using $r_c = 1.414$ nm for KCL [33], $\rho_c = 1980$ kg/m³ as the density, $\frac{m_s}{m_{sol}} = 0.2539$ [34] at S_{25} and a density of $\rho_s = 1178$ kg/m³ [35], the radius of diffusion R is determined from:

$$R = r_c \sqrt[3]{\frac{\rho_c m_{sol}}{\rho_s m_s}}. \quad (2.17)$$

Using the KCl diffusivity of $D = 0.00187$ (nm)²/ps [35] (picosecond), it is found that particles for a crystal are found in an initial region of radius $R = 2.64$ nm. This radius yields a pulse duration of $\Delta t_p \geq 9 \cdot 10^2$ ps as the minimum pulse duration. The minimum pulse duration is longer than the pulse duration used in successful fs (femtosecond) pulse NPLIN experiments, such as those performed by Nakamura *et al.* [36]. Nonetheless, according to TSN, there are local clusters with higher electrolyte concentrations, potentially lowering the required pulse duration for DP based nucleation.

DP adequately explains the modest dependence on λ on NPLIN experiments because the relative permittivity of the particle ε_p depends on λ [37]. Peculiarly, no mention of polarisation switching was found in the DP articles studied for the above derivation. By contrast, polarisation switching is a well-known effect in the nucleation of ferroelectric materials, where the external electric field determines the internal polarisation during the process of nucleation or deposition [38]. Although the processes for NPLIN are somewhat different from DP of ferroelectric materials, the effect of the electric field for different polarisations may be quantified upon the development of a topological theory of DP, taking into account the 3 dimensions of space and the dimension of time.

It was mentioned by Alexander & Camp [39] that the observed threshold intensity $I_{threshold}$ for nucleation might be caused by the fact that a weak field intensity would have no effect. However, this is in conflict with the intensity derivation above, where the full intensity is taken into account. Knott *et al.* [40] suggests that it is due to the absorption of photons by the water. This would imply a correlation between the laser path length in water and $I_{threshold}$, which is in conflict with experimental observations [23]. Potentially, the first effect of the electric field is to induce migration of molecules before any rates can be enhanced through the DP effect.

2.2. Mechanism II: Optical Kerr Effect

The OKE was the initially proposed theory by Garetz *et al.* [17] for the first observed NPLIN phenomena. It was speculated that the polarisation of the laser pulse would cause a transient alignment of the solute molecules by causing induced dipole moments. Sun *et al.* [41] proposed an alignment along the laboratory coordinates $\{x, y, z\}$ using order parameters $K_i = \langle \cos^2(\theta_i) \rangle$, where $i \in \{x, y, z\}$ and θ_i is the angle between a molecular axis having unit vector $\mathbf{a} = (a_x, a_y, a_z)$ - i.e. the alignment of the molecular polarisation - and a laboratory axis i . The polarisation may be represented by an ellipsoid, where the shape depends on the alignment of the molecular building blocks. A polarisability α of a molecule gives rise to an interaction energy of $\Delta E = -\frac{\alpha}{2} \mathbf{E} \cdot \mathbf{E}$, yielding order parameters of

$$K_i = \frac{\int a_i^2 e^{\Delta E/(k_B T)} d\Omega}{\int e^{\Delta E/(k_B T)} d\Omega}, \quad (2.18)$$

where $d\Omega$ ensures integration over all possible orientations of \mathbf{a} . In the absence of an external electric field ($\mathbf{E} = \mathbf{0}$), molecules are expected to have random orientations, so that $K_x = K_y = K_z$. Examples of the alignment of rods and disks for absence of light, linearly polarised light and circularly polarised light are displayed in Figure 2.2.

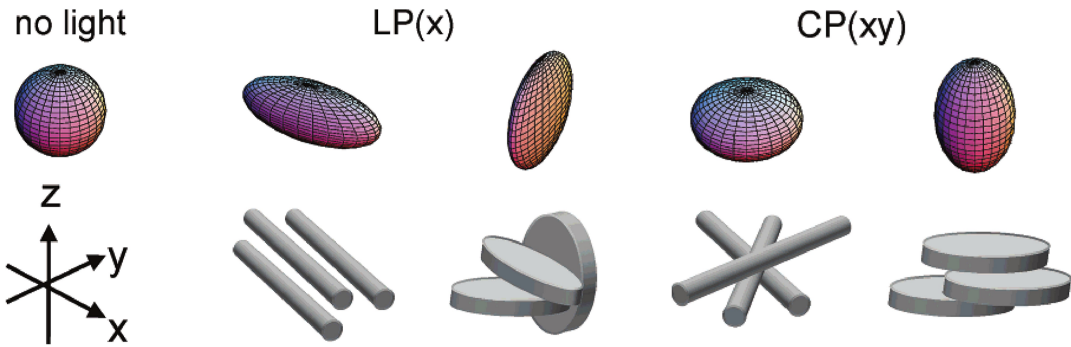


Figure 2.2: The representations of rod-like and disk-like molecules of an electric field parallel to the z direction and i) a linear polarisation in the x direction and a circular polarisation in the xy -plane. Note that the disks rotate when exposed to a linear polarisation, whereas the rods rotate when exposed to a circular polarisation. Image adapted from Sun *et al.* [41].

The order parameters of Equation 2.18 take the form

$$K_i = \frac{1}{3} + \frac{\beta \Delta \alpha E^2}{k_B T}, \quad (2.19)$$

where $\beta \in [0, 1]$ is a coefficient and $\Delta \alpha$ is the difference in polarisation along the axis of light polarisation and the axis perpendicular to this rotation axis, both in the plane of polarisation. Note that an oscillating electric field can obtain a linear polarisation, a circular polarisation or elliptical polarisation [27]. The consequence of

the OKE is that molecules will obtain a particular polarisation, which explains why molecules may crystallise into a specific morphology. Furthermore, simulations of OKE based NPLIN using a Potts lattice gas model show that the induced orientational bias can reduce the free energy of nucleation in addition to promotion of precritical nuclei [40], making it compatible with both CNT and TSN.

However, the OKE mechanism faces two major shortcomings. First, NPLIN has been observed for many compounds without a polarisation, such as many halide salts [6] and even CO₂ vapour bubbles [40]. Secondly, typical laser electric field intensities yield only marginal deviations from $K_i = 1/3$. Taking glycine as an example, $\Delta\alpha = 2 \cdot 10^{-40}$ F m and a typical electric field of $E = 3 \cdot 10^7$ V m⁻¹ result in $\Delta\alpha E^2 = 2 \cdot 10^{-5} k_B T$. As stated in Chapter 1, relevant energies should not be below $k_B T$ by several orders of magnitude. Knott *et al.* [40] have employed Monte Carlo simulations to show that such an energy contribution is unlikely to have significant consequences. Furthermore, in recent studies, correlations between the light polarisation and molecular polarisation were not successfully reproduced [22, 42].

2.3. Nanoparticle Heating

In this section, the absorption of electromagnetic energy by nanoparticles will be clarified. The heating of nanoparticles is the first step in both of the theories in the subsequent sections.

As described in Section 1.3, it is likely that any relevant impurities will have radii of $\mathcal{O}(\text{nm})$ or larger for significant amounts of electromagnetic energy to be absorbed. It is customary to use purified water with a resistivity of $\rho = 18.2$ M $\Omega \cdot \text{cm}$ [6], so that little impurities are expected from the solvent itself. As shown by mass spectrometry experiments on the dried solution components, the amount of impurities found in solutions are often nearly identical with the impurity amounts reported on the electrolyte product containers when ultrapure water is used. Iron oxides and phosphates are the main impurities for NPLIN solutions [43]. Further filtration of the prepared solution shows a decrease in the probability of nucleation, whereas no significant changes in the threshold intensities are reported [44, 45]. Dynamic light experiments show a distribution of impurity particle radii around tens of nm for filtered solutions [43]. Solution doping with iron oxide particles leads to an increase of nucleation probability and no significant change in the threshold intensity [43].

A brief calculation shows that intensities in NPLIN experiments are able to heat up nano-impurities by several hundreds or thousands of Kelvins. Assuming a spherical particle and a laser beam intensity of $I = 15$ MW/(cm)², the heat transfer in an exposure time of Δt is given as

$$\Delta E = \pi r^2 I \Delta t, \quad (2.20)$$

so that a particle volume of $V = \frac{4}{3} R^3$ and a volumetric heat capacity of $C_V(T)$ yields the following temperature change ΔT under the assumption of constant C_V :

$$\Delta T = \frac{3I\Delta t}{4RC_V}. \quad (2.21)$$

Taking $R = 2.5$ nm and $C_V = 3.4$ MJ/(m³ K) as the heat capacity of Fe₂O₃ [46] yields $\Delta T = 2200$ K. Given that for a first order approximation $\Delta T \propto 1/R$, determining the particle size distribution for experimental solutions will be useful for investigation of nanoparticle based NPLIN theories. Although major assumptions are made for this derivation and most materials would readily melt for such temperature elevations, the calculation shows that NPLIN intensities are high enough to cause local evaporation of cavities, as threshold evaporation temperatures vary around 600 to 800 K [43].

The existence of cavities in solutions exposed to lasers in addition to the so-called *cavitation cycle* has been captured both experimentally and in modelling, with time scales varying from ns to ms (milliseconds) and length scales varying from nm to μm [47–50]. The mechanism induced by exposure to a laser beam is visualised in Figure 2.3, where details concerning the evaporative layer and the shockwaves will be discussed in sections 2.4 and 2.5, respectively.

Initially, an impurity particle is assumed to be at equilibrium in a solution, with a homogeneous electrolyte concentration, as seen in Figure 2.3. a) Upon lasing the solution, the particle will absorb electromagnetic energy by excitation of electrons and the increased temperature will cause rapid evaporation of the surrounding solution. In subsequent steps, the impurity will cool down by convection, advection and some diffusion [51]. b) The liquid will start evaporating in an evaporative layer at the vapour-liquid interface and the expanding cavitation bubble causes a shockwave. c) Once the maximum bubble size is obtained, the cavitation bubble is momentarily stationary. d) The cavity will shrink until collapse. e) Another shockwave is generated upon collapse of the cavity. Although the clusters are shown in the last image only, determining when and where these clusters will form will require experimental observation.

Cavity reformation and collapse cycles have been observed experimentally, known as rebounds [50, 52]. The number of rebounds depends on the medium and the thermal energy added to the particle. If the liquid-phase separation is global, a cavity will form and expand, with a significantly lower total particle density in the vapour phase. If the phase separation is spinodal, the solvent evaporates locally and there can be multiple vapour-liquid interfaces.

The mechanism based on concentration caused by the cavity is described in Section 2.4, followed by a description of the mechanism relying on pressure gradients in Section 2.5. For the impurity based theories, is particularly important to verify whether intensities used in experiments are within the experimental range displayed in Figure 1.2, as high addition of energy through impurities may quickly eliminate features of NPLIN.

2.4. Mechanism III: Cavity-Induced Concentration Enhanced Nucleation

The mechanism of CICEN is based on the notion that the cavitation cycle increases the concentration somewhere in the solution until the solution becomes labile at the particular locus, so that nuclei are formed and may start to grow. Such a locus should be regarded as being at a fixed radial displacement from the nanoparticle in the absence of a cavity, or at this particular displacement from the liquid-vapour interface in the presence of a cavity. A three-step mechanism was proposed by Uwada *et al.* [51] for glycine crystal generation on a thin gold film surface and is displayed in Figure 2.4 a). Assum-

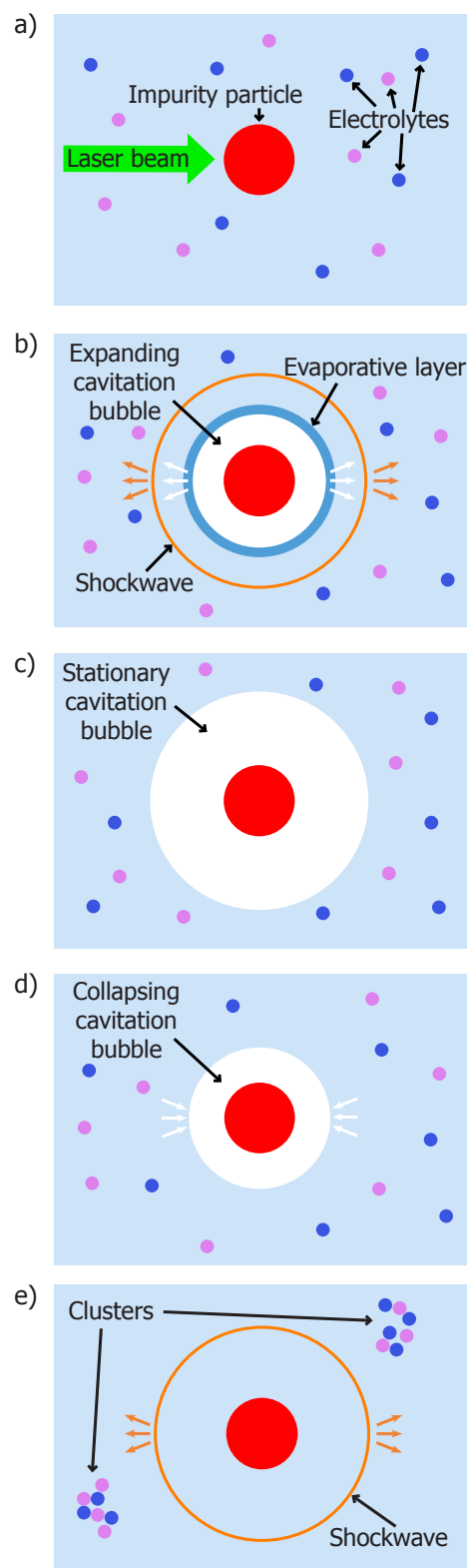
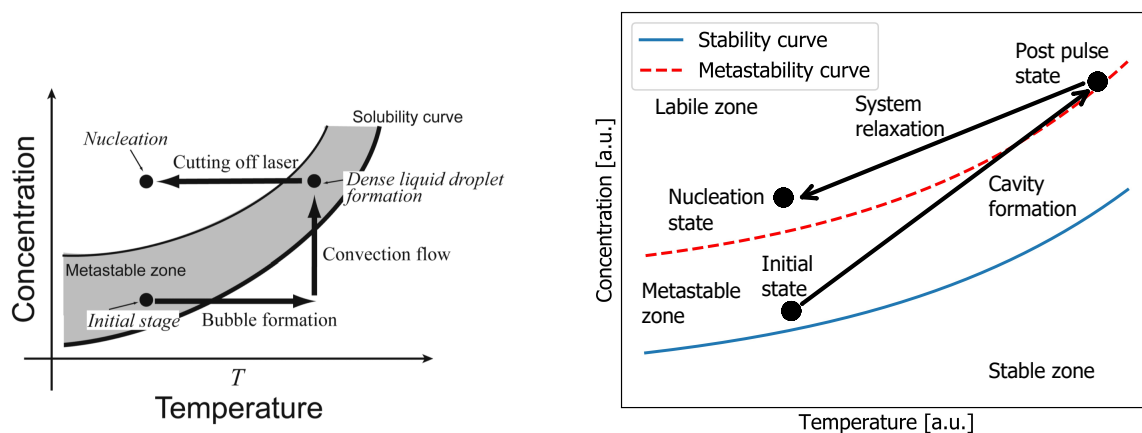


Figure 2.3: Schematic display of the cavitation cycle. The different steps are explained in the text.

ing an incompressible solution, a moving vapour-liquid interface would thrust move the surrounding solution further into the bulk. During binodal evaporation, the solute molecules in the evaporative layer will have to move into the adjacent solvent layer, increasing the concentration locally. Consequently, it is suggested here that the temperature and concentration will rather follow a two-step process, as depicted in Figure 2.4 b).



(a) Top figure: A three step mechanism for concentration enhanced nucleation. Note that the enhanced concentration is induced by convection, which is itself caused by a concentration gradient. The temperature only decreases after the laser pulse is removed. Image obtained from Uwada *et al.* [51].

(b) Bottom figure: A two step mechanism for concentration enhanced nucleation. During cavity formation, both the concentration and the temperature will increase. However, the lability is induced by a higher relative decrease of temperature compared to concentration.

Figure 2.4: Two possible concentration pathways for a point at a particular distance from the cavity or particle boundary.

Two things can be deduced from the above description of the CICEN. Firstly, it is likely that the locus can be still be moved into the labile zone when starting from a stable concentration below the stability curve. Consequently, experiments could be performed with a range of concentrations near the stability curve in order to rule out mechanisms which are unlikely to yield nucleation at undersaturation, such as DP and OKE. Such experiments may be assisted by measuring the transmissivity of the solution during the experiment because crystals could form and redissolve in the undersaturated solutions without having grown to a visible size. Secondly, the three-step mechanism of Figure 2.4 suggests a correlation between I and the width of the MSZW. Consequently, experiments may be performed in order to correlate the MSZW of different solutes to their nucleation probabilities or intensity thresholds. According to the given description of CICEN, a negative correlation between the MSZW and the threshold intensity is hypothesised if the MSZW for the compounds is determined at identical cooling rates.

It is currently unknown whether the nucleation occurs in the surrounding bulk, the vapour-liquid interface or even within the cavitation bubble, perhaps at the nanoparticle as a site for heterogeneous nucleation. In a study by Soare *et al.* [50], optical disturbances were found within the cavitation bubble itself, whereas the nuclei appear at a later stage near the point of these disturbances. However, insufficient information is found in the article to conclude whether the intensities fall within the experimental range mentioned in Section 1.3 because the area of exposure (AoE) of the used microscopic objective is not mentioned. Regardless, the formation of aggregates is also observed in recent MD simulations at temperatures of 5000 K to 10000 K [53] and even at temperatures of 2500 K [54], in agreement with the calculation of Equation 2.21. A mesoscopic model was developed by Soare [55] where it was assumed that the crystals would only form in the bulk fluid. However, such an assumption will require experimental validation.

2.5. Mechanism IV: Cavity-Induced Pressure Enhanced Nucleation

The fourth mechanism relies on pressure enhanced nucleation. First, it is considered how any pressure differences can arise and how they can affect the solution. Kacker *et al.* [44] ruled out the possibility of pressure waves originating from the vessel itself as masking the vessel nullified any nucleation phenomena, despite measuring a higher induced pressure of about $\Delta P = 200$ mbar measured using a piezo-electric transducer just below the air-liquid interface in the vial. However, the data is provided with the transducer at a single location and may vary at different locations in the fluid. If the pressure differences are caused by shockwaves

formed by cavitation bubbles, it should be investigated whether these pressure differences are large enough to induce nucleation according to Equation 1.6. Furthermore, the velocity is denoted as acoustic at a velocity of $v_p = 1383 \text{ m s}^{-1}$, which is only slightly below the sound velocity at saturated KCl solutions of $v_s = 1468 \text{ m s}^{-1}$. Here, v_p is based on an assumed distance of the transducer to the origin, despite the possible variability of the cavitation source in NPLIN experiments. As velocities above v_s can cause shockwaves which can easily lead to nucleation, the mechanism of CIPEN mechanism will be investigated further below.

According to CIPEN, pressure changes originate from cavitation bubbles, either as sound waves or as ultrasound waves or shockwaves. The formation of pressure waves is a well-established phenomenon in the literature [56, 57]. Usually, the shockwaves are generated the origination and collapse of the vapour bubble, as displayed in Figure 2.3. Moreover, polarisation effects are sometimes attributed to the pressure effects. Lui *et al.* [22] conducted experiments on the nucleation of glycine and pointed out ratios of α - and γ -polymorphs that were similar over a saturation range for sonocrystallisation, mechanical shock and NPLIN. The increase in the γ -fraction with increasing supersaturation was attributed to local higher concentration in relation to cavitation bubbles, which would favour the formation of γ -glycine, providing an alternative explanation for the effects.

2.5.1. Pressure Contributions to the Chemical Potential

The shockwaves are seen as a plausible mechanism for many NPLIN experiments by some authors [15, 58, 59]. The significance of involved pressure changes can be evaluated through the change in $\Delta\mu$ according to Equation 1.6, where the pressure increase should exceed the effect of the temperature increase. Tagawa *et al.* [60] provide an account of measured pressure changes through the formation of a cavity, documenting specifications of involved components that allow for calculations based on the data. The article contains a description of pressure measurements at a range of microscopic objectives and laser pulse energies for $\lambda = 532 \text{ nm}$ and a pulse duration of $\Delta t = 6 \text{ ns}$. In the following calculation, the effect of ΔP on $\Delta\mu$ is provided for the lowest I data found in the article from Tagawa *et al.*. Notably, the resulting waves will be acoustic because measured pressures remain well below the shockwave threshold of $\Delta P_{shock} \geq 200 \text{ MPa}$ [61]. As a result, pressure waves are acoustic and cannot travel fast enough to avoid any effect of ΔT . The minimum AoE diameter d for a focused beam follows from the diffraction limit [62]:

$$d = 1.22 \frac{\lambda}{NA}, \quad (2.22)$$

where $NA = f/D$ is the numerical aperture in terms of the focal length f and the diameter D of the lens entrance pupil. NA was 0.10 for the 5x microscope objective, yielding $d = 6.5 \text{ }\mu\text{m}$. For a Gaussian laser beam, the beam diameter is given as [27]:

$$d = \frac{2\lambda}{\pi NA}. \quad (2.23)$$

However, the Intensity calculations by Tagawa *et al.* [60] are based upon Equation 2.22. Additionally, the lowest pulse energy used was $\Delta E = 2.6 \text{ mJ}$, so that $I = 1.3 \text{ TW}/(\text{cm})^2$, which is roughly 5 orders of magnitude larger than typical intensities used in NPLIN experiments. As a consequence of such a pulse, peak pressures of $\Delta P \approx 0.2 \text{ MPa}$ were observed. In order to estimate the change in the chemical potential, the effect the volume change V will be approximated. Similar to the derivation in Subsection 2.1.1, the initial volume is assumed to be a region that provides sufficient particles for the formation of an assumed spherical crystal of radius r_c . Taking KCl as an example again, it is known from Section 2.1.1 that $R = 2.64 \text{ nm}$ and $r_c = 1.414$. From this, the new volume equals that of the crystal radius and the remaining water volume as

$$V_{new} = V_{crystal} + V_{water} = \frac{4\pi r_c^3}{3} + \frac{4\pi R^3 \rho_s}{3\rho_{H_2O}} \cdot \frac{m_{H_2O}}{m_{H_2O} + m_s}, \quad (2.24)$$

where $m_{H_2O}/(m_{H_2O} + m_s)$ is mass fraction of water in solution. Equation 2.24 is valid under the assumption that the solution density scales linearly with the amount of added KCl, which is approximately valid for the concentrations considered here [63]. The volume difference for the given parameters is $\Delta V = 2.61 \cdot 10^{-9} \text{ (nm)}^3$. At the maximum observed pressure change of $\Delta P \approx 0.2 \text{ MPa}$, the change in chemical potential for a shock wave while disregarding any temperature changes is $\Delta\mu \approx \Delta V \Delta P = 3.1 \text{ meV} = 0.12 k_B T$. Therefore, significant pressure effects would require intensities approximately 5 orders of magnitude above typical NPLIN intensities. Related temperature effects of the nanoparticle heating would further lower the nucleation probability.

3

Experimental Methods

In this chapter, the experimental setup will be described. The used software is described in Section 3.1. The laser setup is described in Section 3.2. The operation of the camera software and post-processing of images is described in Section 3.3 and the preparation of samples is described in Section 3.5. Lastly, the setup used for obtaining data on the MSZW is described in Section 3.6. The chapter is intended to provide sufficient details to make the experiments reproducible with a minimum amount of effort.

3.1. Software

All of the figures in this paper were created using Adobe InDesign®, whereas all the graphs were created using Python® [64], unless otherwise mentioned. Images and videos were captured using PCO Camware 4® [65], and all image post-processing was performed with Mathworks MATLAB® [66].

3.2. The Laser Setup

A schematic overview of the laser setup is provided in Figure 3.1.

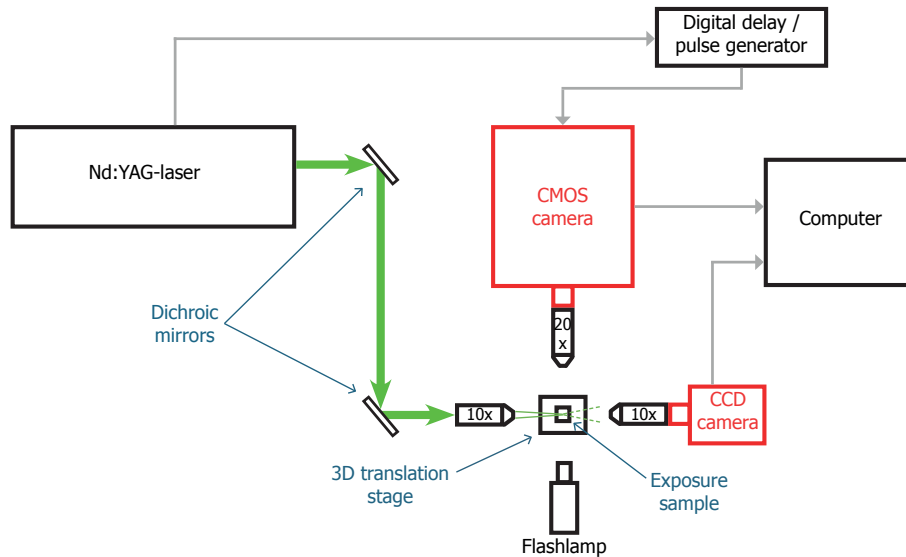


Figure 3.1: An overview of the different components in the laser setup. The laser beam reflects off of two dichroic mirrors and passes through a 10x objective before reaching the exposure sample placed on a 3D translation stage and illuminated by a flashlamp. The CMOS camera detects events through a 20x objective and the CCD camera records the area of exposure through a 10x objective. The laser controller activates the digital delay / pulse generator, which triggers the camera, ensuring that transmitted images are being recorded. The gray arrows denote the image triggering sequence.

The dichroic mirrors are used for suitable positioning of all of the components on the optical table. Upon firing the laser, a pulse is transmitted from the laser controller to a Stanford Research Systems Model DG535 digital delay / pulse generator [67]. If the generator is programmed to trigger externally, a trigger pulse is sent from the external trigger BNC-connector into the "acq enbl" (not the "exp trig".) BNC-connector of a CMOS (complementary metal oxide semiconductor) camera. Subsequently, a sequence of images is transmitted from the camera to the computer and denoted as an imaging sequence. The laser used for the experiments is a Continuum Powerlite DLS8000 ND:YAG(Al_2O_3) laser [68] with a cross-sectional area of $A = 20 \text{ mm}^2$, repetition rate of $\nu = 10 \text{ Hz}$, $\lambda = 532 \text{ nm}$ and a pulse duration of $\Delta t = 7 \pm 1 \text{ ns}$. The laser and generator are displayed in Figure 3.2.



(a) The Continuum Powerlite™DLS8000 laser ND:YAG(Al_2O_3) laser. Full specifications can be found in the product data sheet [68].



(b) The Stanford Research Systems Model DG535 digital delay / pulse generator which is used for triggering the recording of an image sequence. Full specifications can be found in the service manual [67].

Figure 3.2: The components used for lasing solutions and triggering events in the laser setup.

Additionally, a CCD (charge-coupled device) camera was positioned on the axis of the laser beam axis or optical axis for determining the AoE. the CMOS camera was mounted horizontally with its imaging axis perpendicular to the optical axis. Carl Zeiss EC "Plan-Neofluar" 10x/0.3 (magnification/NA) M27 objectives were mounted on the laser beam path and in front of the CCD camera for focusing and a Carl Zeiss EC "Plan-Neofluar" 20x/0.50 M27 objective was mounted in front of the CMOS camera. Wavelength filters were placed between the objectives and cameras, to prevent damaging of the lenses.

An exposure sample could be placed on a translation stage which allowed for translating the sample in 3D at the μm scale. A flashlamp was placed to illuminate the sample and it was verified that the lamp did not cause measurable heating of the samples. The pulse energy was determined by exposing a laser beam profiler and the output energy and pulse duration can be displayed on an oscilloscope. The laser beam intensity was lowered using Q-switching, where the light in the optical resonator of the laser is attenuated before leaving the laser. The laser intensity should be lowered such that the focused beam is at intensities suitable for NPLIN experiments because a laser beam that is not Q-switched can potentially damage the objectives over time [69].

It was found that the laboratory temperature could fluctuate from $T = 20 \text{ }^\circ\text{C}$ up to $T = 28 \text{ }^\circ\text{C}$ during experiments. Therefore, vials and cuvettes were stored in a water bath at $T = 25 \text{ }^\circ\text{C}$. During experiments, vials or cuvettes were taken out one at a time, dried carefully on the sides, potentially exposed and then placed back in the water bath. It was decided that control samples should undergo the same procedure with the exception of firing laser pulses. Otherwise, a smaller amount of control vials might nucleate spontaneously due to less handling of the samples. Before experiments, prepared samples were cooled down to $T = 25 \text{ }^\circ\text{C}$ in the water bath at cooling rates of $1 \text{ }^\circ\text{C} / \text{min}$, which did not appear to cause nucleation for any of the involved solutions.

3.3. Imaging settings

The NPLIN phenomena can be captured using an ultrahigh speed camera which can captures images at rates of $\mathcal{O}(10^5 \text{ fps})$. For this purpose, a PCO Dimax S4 CMOS camera [70] was selected. Additionally, the AoE was determined using a high speed Mikrotron Eosens CCD camera [71].

Camera software options in this paragraph are denoted in *italics* and proposed imaging settings for these options are denoted in **bold**. The *Trigger Mode* should be set at **Auto Sequence** and the *Master/Slave Mode*



(a) The PCO Dimax S4 ultrahigh speed camera used for imaging the cavitation phenomena. Full specifications of the camera are found in the product data sheet [70].



(b) The Eosens 3CL high speed camera used for imaging of the Area of Exposure. Full specifications of the camera are found in the product data sheet [71].

Figure 3.3: An overview of the cameras used in the experiments. During the experiments, objectives rather than lenses are placed in front of the camera chips, with optical light filters to prevent damaging of the chips.

should be turned **Off**. Setting the *Recording Mode* at **Ring Buffer** ensures that the camera will overwrite its own memory until a recording event is triggered. The *Sequence Trigger Mode* should be set to **Ext. or Soft Event** to allow triggering by the camera or by the PCO Camware 4 recording button. The *Images Before T₀* denote the images made before the triggering event and the *Images After T₀* denote the images made after the triggering event, whereas the total of these images will ensure filling of the allocated *RAM Segment*. the *FPS Control Mode* ensures that the region of interest (ROI) is maximised for a given frame rate. Connecting the camera to the PC using a Cat5e or Cat6 cable ensures that the data transmission rates through the cable exceed the data acquisition rates of the camera and the *Package Delay* can be set at **40**. Notably, updating the graphics card driver on the PC caused the camera software to crash frequently, so that a rollback was performed.

3.4. Post-processing

The mechanism of a CMOS camera involves detecting charges on parts of a chip [72] which can be excited by light. However, CMOS cameras will often detect some static charges on the chip, even in complete absence of light. As a result, a CMOS camera image generally has an undesired bar pattern on its images, especially near the centre of the image. To remove these patterns, so-called *dark frames* are made at low intensities and they are subtracted pixel by pixel from pre-processed images, known as *dark image subtraction* [73]. An intensity correction is applied during the processing to correct for the loss of intensity from the dark frame subtraction.

The inline code below shows how the post-processing can be achieved in MATLAB. The user has to provide the file names of the background image, image sequence and intended filtered image sequence files between brackets, in addition to the desired intensity increase number $\in [0..100]$ and the number of files in the image sequence. If all of the required files are present in the folder of execution, MATLAB writes the images files in target image file (TIF) format in the folder where the script is executed. In the example, the background file name is 'background.tif', the unfiltered sequence image names are 'image1.tif' to 'image10.tif' and the sequences will be saved with names from 'saved1.tif' to 'saved10.tif' and the image intensity will not be corrected.

```

% This script is intended for post-processing of sequences of tif-files for
% the generation of noise free videos. Written by Tom van Waas in 2019.

% Parameters required from the user
backname = num2str('background') ; % Name of background image
sequence = num2str('image')       ; % Name of image sequence
savename = num2str('saved')       ; % Name of filtered sequence
brighten = 0                      ; % Brightness increase number
num_file = 10                    ; % No. of files

% Post-processing part
back = strcat(backname, '.tif')    ;
back = imread(back)               ;
% This loop filters the image and subtracts brightness
for i=1:num_file
    figure = strcat(sequence, num2str(i), '.tif') ;
    figure = imread(figure) + brighten ;
    final = imsubtract(figure, back) ;
    imwrite(final, strcat(savename, num2str(i), '.tif')) ;
end

```

3.5. Sample Preparation

For the experiments, KCl, NH₄Cl and NaCl were used. Attempts at making a supersaturated NaCl solution were unsuccessful. It was found that that MSZW for NaCl is remarkably thin, making it difficult to obtain a supersaturated solution of NaCl. The salts used in the experiments of this paper are displayed in Table 3.1.

Table 3.1: Overview of the different chemicals used during the experiments of this paper.

Name	Chemical formula	CAS registry number	Purity [%]
Potassium chloride	KCl	7447-40-7	≥ 99.5
Sodium chloride	NaCl	7647-14-5	≥ 99.5
Ammonium chloride	NH ₄ Cl	12125-02-9	≥ 99.8

Samples were prepared by adding electrolyte solutions to vials or cuvettes. Borosilicate vials were cleaned with $\rho = 18.2 \text{ M}\Omega \cdot \text{cm}$ conductivity water and dried. 200.0 g of $\rho = 18.2 \text{ M}\Omega \cdot \text{cm}$ water was added to the vials. Afterwards, an amount of salt was added that would lead to the desired $S_{25} \in [1.0, 1.1]$. Solutions were placed in the oven at $T = 65 \text{ }^\circ\text{C}$ until the salt had visibly dissolved and was retained in the oven for at least two more hours. The additional retention time may allow for the dissolution of crystals which are no longer visible, but which are still larger than the critical radius of the compound.

The solution was then transferred to 15 mL storage vials using a 50 mL syringe. Later, the solution could be transferred further into cuvettes and exposure vials. Although it is customary for NPLIN experiments to use transfer materials only once, it was found that reusing pipettes for filling an entire batch of containers did not increase spontaneous nucleation rates if the transfer was performed with recently heated solutions.

Although cylindrical vials are common in NPLIN experiments, the cylindrical shape would both defocus any focused laser beams and distort any images from the camera. Consequently, it was decided that square cuvettes would be more suitable for the imaging experiments. The cuvettes were required to be thin-walled and all cuvette sides would have to be transparent, so that light on both the optical and imaging axes would be largely unhindered. Cuvettes were selected of internal dimensions 1 cm x 1 cm x 4 cm as the depth, width and height as sufficiently large exposure volumes for bulk experiments.

Several materials were tested as potential candidates for NPLIN experiments. Glass materials were found unsuitable because the transmissivity of glass is only sufficient at high quality glass, which would have to be reused for financial purposes. It was also found that plastic cuvettes consisting of PS would absorb laser light at NPLIN intensities, leading to damaging. However, PMMA showed no sign of any adsorption at NPLIN intensities and was used throughout all subsequent experiments.

After the final transfer of solution, samples should be heated to redissolve any crystals from the transfer. The cuvettes were sealed with a cuvette cap to prevent evaporation. Cuvettes were marked at the volume height to track evaporation in the oven. For the first experiments, the cap was attached using Norland Optical Adhesive, which cures during exposure to UV light. However, this did not prevent observable evaporation in the cuvettes. The cuvettes were then sealed using RS PRO white acrylic sealant paste [74]. It was found that the sealing compound prevented visible amounts of evaporation if the cuvette was allowed to rest for 3 days

before being placed in the oven. Interestingly, no visible evaporation occurred if the heating in the cuvettes was executed in a water bath rather than in the oven. Although the cuvette brim was kept above the water level in the bath at all times, the humid air in the water bath may have prevented significant evaporation of the cuvettes. The cuvettes, caps and sealing compound are displayed in Figure 3.4.



(a) The cuvettes and a sealing cap, which were used for the imaging experiments. The cuvettes were transparent with a thickness of approximately 1 mm.



(b) The sealing compound used for attaching the caps to the cuvettes, thereby sealing the cuvettes.

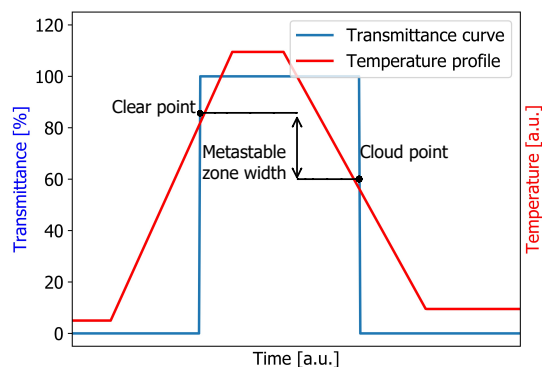
Figure 3.4: The exposure vial materials used for the imaging experiments.

3.6. Metastable Zone Width Determination

It was attempted to determine the MSZW for the salts listed in Table 3.1. The MSZW can be obtained by measuring nucleation and dissolution temperatures via the transmissivity over a programmed temperature profile. The experiments were performed using a Crystal16 device, which is displayed in Figure 3.5 a), whereas a typical temperature profile is displayed in Figure 3.5 b).



(a) The Crystal16, which allows for transmittance determination data for different temperature profiles. The can hold up to 16 vials in 4 temperature profile blocks, which can contain 4 vials each.



(b) An idealised transmissivity curve for a specific compound against programmed temperature profile. The transmissivity goes to 100% upon dissolution at the clear point and goes to 0 upon crystallisation at the cloud point.

Figure 3.5: Equipment for the generation of the stability and metastability curves for various compounds.

In the Crystal16, the transmissivity is measured during the temperature cycle. If the temperature maximum is sufficiently high, crystals may dissolve at a particular temperature during the temperature decrease, determining the *clear point* on the solubility curve at a given concentration. If the temperature minimum is sufficiently low, crystals may nucleate at a particular temperature during the temperature decrease, determining the *cloud point* on the metastability curve at a given concentration. For the experiments, vials were placed in the Crystal16 per 4 vials. A magnetic stirrer was placed in the vials to ensure sufficient mixing at a stirring rate of 700 rpm. Vials were cooled at a rate of 5 °C/h. Metastability data dependence on temperature decreases with the cooling rates, allowing for comparison of metastability data at low cooling rates [75].

4

Results & Discussion

In this chapter, the experimental results are discussed. Initial lasing experiments were aimed at creating an image sequence of the cavitation event in order to trace nucleation phenomena. Additionally, vials were exposed to quantify the nucleation probability in terms of the number of pulses, the intensity for two different solute molecules, namely KCl and NH_4Cl . Unfortunately, the laser went under unexpected maintenance, so that data was only obtained for some intensity values in relation to the number of exposure pulses. This chapter is divided into three sections. The experimental range data and the exposure results are presented in Section 4.1, the results of the image post-processing are found in Section 4.2 and the metastability data is provided in Section 4.3. All results are displayed with 95% confidence intervals for the standard uncertainties, as calculated in Appendix A.

4.1. Laser Intensity Results

First, the AoE of the focused beam was determined. The CCD camera was mounted on the optical axis as displayed in Figure 3.1 and a glass sheet of width $w = 0.1$ mm was placed on the 3D translation stage. Subsequently, the piece of glass was exposed to laser beams of various intensities until the threshold intensity for solid ionisation was found. The laser intensity was lowered using Q-switching and using the laser beam profiler, it was found that the pulse duration was $\Delta t = 15 \pm 1$ ns and threshold intensity for optical breakdown of the glass at $I_{threshold} = (1.4 \pm 0.1) \cdot 10^2 \text{ MW}/(\text{cm})^2$ was found.

This threshold agrees with the observation that NPLIN experiments are performed with experimental intensities below $\mathcal{O}(100 \text{ MW}/(\text{cm})^2)$ [44, 76]. Subsequently, a beam diameter of $d = 50 \pm 3 \mu\text{m}$ was found, which corresponded to 17 pixels of the CCD camera at the given magnification. The large uncertainty in the beam diameter is the consequence of the magnified resolution of the camera and may be improved by using an objective with a larger magnification or a camera with a higher resolution.

At $I = 1.3 \pm 0.1 \cdot 10^2 \text{ MW}/(\text{cm})^2$ no damaging of the glass sheet was caused. This sudden disappearance of any effect at a somewhat lower intensity may be explained in terms of the spot size. The intensity at the centre of a Gaussian beam is given by an Airy disk, with a point spread function displayed in Figure 4.1.

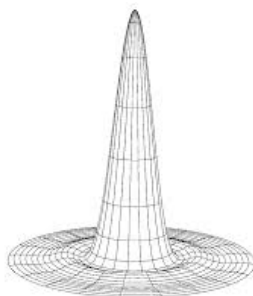
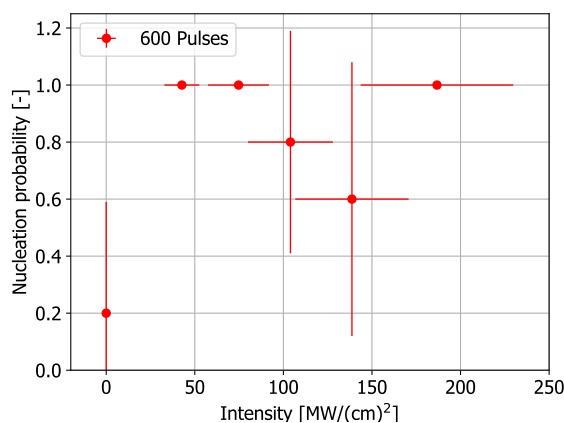


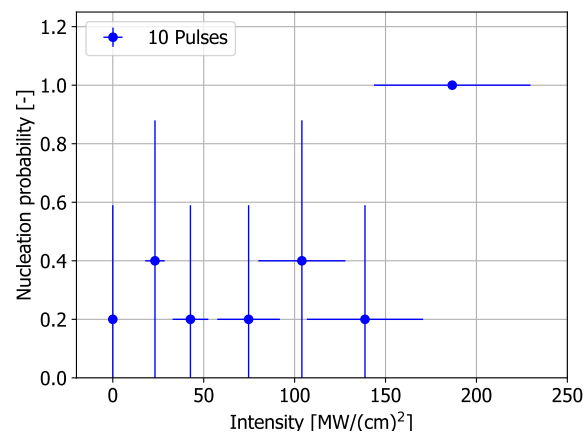
Figure 4.1: Radial point spread function of the Airy disk. The sharpness of the peak increases with the focusing of the beam. Image obtained from [77].

For a high numerical aperture, the plateau may be even wider [27]. Such a high laser beam plateau explains why the width of the damaged spot changes abruptly with I . Notably, the beam is a lot wider than the diameter of $d = 1.1\mu\text{m}$ predicted by Equation 2.23. It is likely that the beam is widened by the imperfections of the optical system. In particular, the cuvette wall and different refraction index n of the solution can defocus the beam.

The nucleation probability p for a $S_{25} = 1.05$ solution was determined for different intensities and a different number of pulses, both at a pulse rate of $\nu = 10$ Hz. 5 Vials per intensity were exposed to 600 pulses at 5 different intensities and 5 vials per intensity were exposed to 10 pulses for 6 different intensities. For both of the experiments, 5 control vials were not exposed to the laser. The nucleation probabilities are displayed in Figure 4.2.



(a) The nucleation probability versus the pulse intensity for samples exposed to $n = 600$ pulses.



(b) The nucleation probability versus the pulse intensity for samples exposed to $n = 10$ pulses.

Figure 4.2: The nucleation probabilities for 600 and 10 pulses, respectively. The results are discussed in the text.

Out of the 10 control vials from the number of pulse experiments, two vials had undergone spontaneous nucleation. Although it is unclear whether this spontaneous nucleation was due to the handling, it was noted that all control vials should undergo the same handling procedure with the exception of exposure to the laser, in order to account for spontaneous nucleation due to handling procedures.

The uncertainty in I increases linearly with the intensity due to the propagation of uncertainties. The uncertainty in I can be decreased by determining d more accurately by measuring the AoE with an objective of a larger magnification. Notably, the standard uncertainties are always 0 for data with $p = 0$ or $p = 1$. However, the magnitude of the standard uncertainties for the given results rule out any conclusions on the relation between p and the number of pulses because 3 out of 5 of the data points with $I < 150$ MW/(cm)² are not significantly different. However, it does suggest that the uncertainties should be sufficiently small for the given experiment at a number of samples of $\mathcal{O}(10)$ or higher. Ionisation was found for the largest two intensity values, which could be recognised as a green flash in the sample in addition to a soft sound.

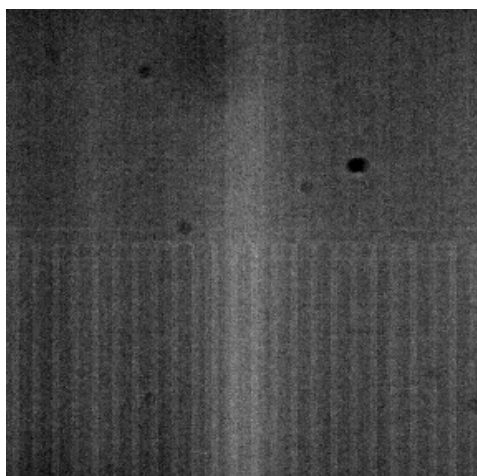
4.2. Image Post-Processing

It was found during the post-processing that the given camera had specifications which would suffice for creating an image sequence. However, using the setup determining the cavitation bubble expansion and collapse rates similar to Sun *et al.* [47] would likely benefit from better camera specifications for capturing the dynamics of cavitation bubbles, which are of $\mathcal{O}(10\ \mu\text{s})$. In recent years, cameras which still provide a proper resolution at corresponding frequencies have become available, such as the Phantom v2512 [78].

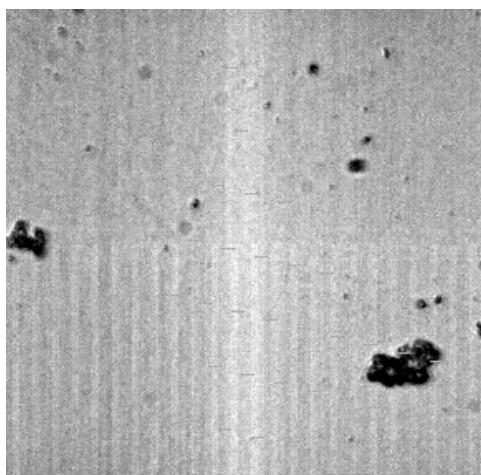
For creating the images, the focus of the laser beam out of the 20x objective was carefully aligned in the centre of the ROI of the CMOS camera. It was found that positioning cuvettes at the same location was important for aligning the laser focus with the centre of the COI. Because the refractive index $n \approx 1.33$ of the solution is somewhat larger than the refractive index of air at $n \approx 1$, the displacement of the laser focus on the optical axis depends on the positioning of the cuvette. This positioning problem could be solved by creating a cuvette holder on the 3D stage, or by performing the experiments on continuous media, such as microfluidic devices, which are readily being developed based on PMMA for nucleation experiments [79].

The system magnification was determined by moving specific items on the translation stage and comparing the displacement on images with the displacement on the stage. The camera has a maximum ROI of 2016x2016 pixels on a chip of 22.18 mm x 22.18 mm, yielding a standard resolution of 11 μm per pixel. With the 20x position in place, a resolution of $0.99 \pm 0.01 \mu\text{m}$ per pixel was found, yielding a magnification of 11.1 ± 0.1 . The system magnification is lower than the maximum magnification of 20x by the objective because the 20x magnification is only obtained when the camera chip is positioned at an infinite distance from the objective. If a better magnification is required with the setup, the camera should be positioned at a larger distance from the back of the objective.

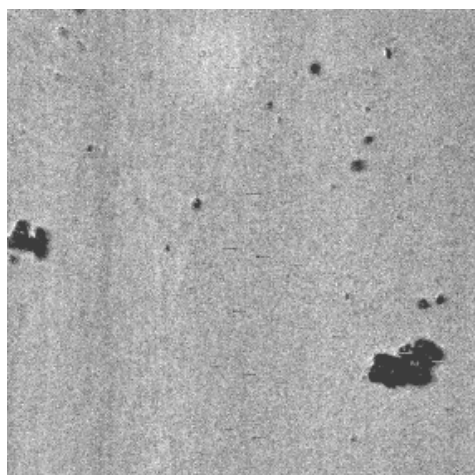
Additionally, it was attempted to remove undesired patterns from images and image sequences. The CMOS bar pattern was found on the images. The pattern was particularly visible for images with a small ROI. In addition, some dust particles on the wavelength filter and camera glass were still visible after cleaning the components thoroughly with optical cleaning cloth. Consequently, the post-processing of images as described in Section 3.4 was applied to the images. A test image was made of some crystals on the wall of a cuvette to verify the image quality improvement. A dark frame, pre-processed image and a post-processed image are displayed in Figure 4.3.



(a) a) The background image or dark frame which is subtracted from the unprocessed images.



(b) b) The image before subtraction of the background image. The larger objects are crystals on a cuvette wall.



(c) c) The image after the background has been subtracted and the intensity has been increased.

Figure 4.3: The effect of post-processing CMOS-images. The final image c) is obtained by subtracting a) from b) and correcting for the loss of intensity.

The post-processing removes the CMOS bar pattern and reduces the visibility of the dust particles on the image. The post-processing can be automated as shown in Section 3.4. Consequently, applying the post-

processing procedure can be useful for improving the quality of images from any imaging setup containing CMOS patterns, whereas it can also be applied generally to images that contain other undesired artefacts from either the hardware or the software.

4.3. Metastable Zone Width Results

Solutions of supersaturations $S_{25} \in \{1.000, 1.025, 1.05, 1.075\}$ were prepared for KCl, NH_4Cl and NaCl and placed in the programme blocks of the Crystal16 in quadruples. Subsequently, a temperature programme of 3 cycles was applied with temperatures of $T \in (10, 50)$ °C with heating and cooling rates of $\pm 0.05^\circ\text{C}/\text{h}$, respectively. It was found that the temperature dependence of NaCl with respect to concentration was not high enough for all of the crystals in the supersaturated solutions to dissolve at the higher temperatures. Consequently, the stability curves and metastability curves were only obtained for KCl and NH_4Cl . The respective curves in addition to literature stability curves and their R^2 values are displayed in Figure 4.4.

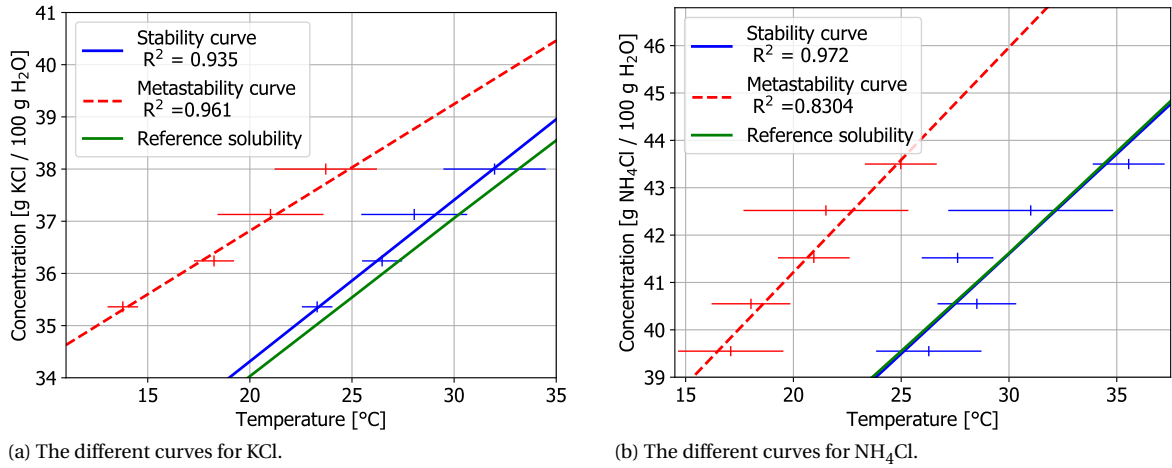


Figure 4.4: Experimental and reference solubility curves together with metastability curves for KCl and NH_4Cl , respectively. The cooling rates were $5^\circ\text{C}/\text{h}$. The MSZW for both of the curves is provided in the text. Solubility and The reference data is obtained from Lide. [46].

The experimental curves are extrapolated linearly below and above the experimental data. The stability data measured with the Crystal16 is in agreement with the reference solubility curves. The vertical uncertainties arise from propagation of uncertainty formulae as calculated in A whereas the horizontal uncertainties originate from dissolution rates and induction times during the temperature cycles, as seen in Figure 3.5 b) for vials at an assumed identical concentration.

c_S and metastability curves c_M with units of g salt / (100 g H_2O) and with T in °C are as follows. For KCl are $c_S = 28.13 + 0.309T$ and $c_M = 31.96 + 0.243T$, whereas for NH_4Cl the equations are $c_S = 28.95 + 0.422T$ and $c_M = 31.72 + 0.475T$. Consequently, at 25°C , the MSZW for KCl is $\Delta c = 2.2$ g KCl / (100 g H_2O) and the MSZW for NH_4Cl is $\Delta c = 4.1$ g NH_4Cl / (100 g H_2O). The observation of a MSZW with a higher thickness for NH_4Cl is in agreement with the observation that there is less spontaneous nucleation for NH_4Cl . However, the MSZW values for these compounds are different, whereas no difference in the nucleation threshold intensity $I_{threshold}$ was found. Consequently, it appears that there is no correlation between the MSZW and $I_{threshold}$. In addition, a plausible explanation for $I_{threshold}$ was found. Ward *et al.* [43] report $I_{threshold} = 5.2 \text{ MW}/(\text{cm})^2$ for a multitude of salts, which is very close to the observed threshold of cavitation bubble formation, found at $I_{threshold} = 5.4 \text{ MW}/(\text{cm})^2$. Although future experiments could be performed to verify that $I_{threshold}$ appears independent of the solutes, the requirement of a cavitation bubble formation is a plausible explanation for $I_{threshold}$ with respect to the currently available data.

5

Conclusions & Recommendations

In this chapter, the conclusions based on the work in this paper are provided in Section 5.1 and the recommendations are provided in Section 5.2.

5.1. Conclusions

For OKE, it has been found that relevant energies are below $k_B T$ by several orders of magnitude. OKE does not explain any of the phenomena for isotropic molecules. Regarding CIPEN, potential effects are only predicted for laser intensities which are above the optical breakdown intensity of solids by several orders of magnitude. It is highly unlikely that OKE and CIPEN are the central mechanisms for NPLIN phenomena, although side effects in conjunction with other mechanisms are not excluded.

For DP, it has been found that the minimum pulse duration Δt_p , required for formation of clusters with radii above r_c , is shorter than pulse durations used in ns laser pulse experiments, although Δt_p is longer than the pulse duration used in fs pulse experiments. Thus, these fs results are difficult to explain using DP. Experimental data for several salts is in good agreement with modelling based on DP equations. Moreover, DP could potentially explain polarisation switching effects because the polarisation axis of light may influence the dielectric polarisation of the molecule. The threshold intensity for DP may be explained in terms of migration of solutes.

CICEN provides an explanation for the observed $I_{threshold} = 5.2 \text{ MW}/(\text{cm})^2$ of nucleation of various salts, which is close to $I_{threshold} = 5.4 \text{ MW}/(\text{cm})^2$ for formation of cavitation bubbles. The mechanism requires further experimental observation to determine whether the nuclei form inside of the cavitation bubble, at the vapour-liquid interface or in the surrounding medium. Polarisation switching explanations related to CICEN may be provided in terms of local supersaturation increases near the cavitation bubble, as the supersaturation is known to influence morphology.

The uncertainty in the intensity data for NPLIN experiments with focused beams is largely a consequence of the uncertainty in the AoE size. The uncertainty in the AoE size can be decreased by observing the damaging effect at $I_{threshold}$ using a camera setup with a better resolution. The uncertainty in the intensity data may account for the discrepancies in reported $I_{threshold}$.

Defining the MSZW as the concentration difference between the clear points and cloud point concentrations at a particular temperature, it is found that the MSZW for KCL at 25 °C is $\Delta c = 2.2 \text{ g KCl}/(100 \text{ g H}_2\text{O})$. In addition, the MSZW at 25 °C for NH_4Cl is $\Delta c = 4.1 \text{ g NH}_4\text{Cl}/(100 \text{ g H}_2\text{O})$. Because no difference in $I_{threshold}$ is found for these compounds, The MSZW appears to be uncorrelated to $I_{threshold}$. The MSZW can still be used to determine whether a chemical compound is suitable for NPLIN experiments conducted with supersaturated solutions.

The central conclusion of this paper is that performing visualisation experiments can effectively be conducted with the described setup, so that spatiotemporal characteristics of the NPLIN phenomena and of the CICEN mechanism can be determined. Several problems related to the setup have been eliminated. Evaporation can be reduced by sealing the caps to the cuvettes and placing the cuvettes in a water bath rather than in an oven. Furthermore, the laser beam focus can be aligned with the camera ROI by translation of the objective on a stage adjustable at μm scales. Misalignment due to a different path optical length on the solution can be reduced by the implementation of a sample holder on the sample translation stage. Post-processing

of images effectively removes CMOS bar patterns and can significantly reduce the visibility of artefacts from impurities on optical components.

Some means of reducing energy and materials reduction have been discovered. It was found that reuse of items utilised for solution transfer such as pipette tips did not lead to a significant increase of spontaneous nucleation of compounds if the transfer was performed with heated solutions. Experiments can be combined with simulations, which do not involve the operational costs of an entire laboratory. NPLIN has also been found suitable for operation in continuous reactors, reducing the required amount of solution and containers.

5.2. Recommendations

The DP theory may benefit from the development of a topological theory, taking into accounts its effects for different polarisations of light. A topological account of DP may allow for determining whether DP is capable of explaining polarisation switching effects.

CICEN should be further investigated with the experimental setup described in this paper. If it is desired to spatiotemporally characterise the cavitation cycle and potential NPLIN phenomena, an ultrahigh speed camera with better specifications might be required for creating image sequences near the intensity threshold for cavitation bubble formation. Additional experiments should be conducted with undersaturated solutions as this is expected to lead to nucleation according to CICEN, whereas it should not lead to nucleation according to DP in combination with CNT.

For visualisation experiments, it is recommended to use NH_4Cl . The growth rate of NH_4Cl appears unprecedented, making it a useful salt for spatiotemporal characterisation of nucleation using visual equipment. NH_4Cl and KCl are suitable salts for NPLIN experiments at supersaturation because of a large MSZW. NaCl is not suitable because the solubility depends weakly on temperature and because of a thin MSZW.

Given the large number of vials required for statistical significance in addition to the difficulty of producing these large numbers in NPLIN experiments, the process of mechanistic understanding would be accelerated by applying open science protocols. Experimentalists could potentially publish their NPLIN exposure data more often.

NPLIN phenomena can be studied more sustainably in microfluidic devices. Such devices can be made of PMMA to avoid damaging by the laser at high intensities. CICEN should still be studied in the bulk phase to avoid any effects of the container walls. For bulk experiments, optically curing compounds can be replaced with sealing compounds which are less expensive and less contaminating.

Some of the current topics in NPLIN problems can be addressed by conducting MD simulations in addition to the experiments. Some of these simulations should focus on the effect of nanoparticle heating. The effect of different polarisations on isotropically polarised molecules can be used for quantifying the effects of DP. Both of the mechanisms could be studied during the same simulation runs for determining whether there are any mechanistic interactions. If the electric field leads to migration of electrolytes, this proposes an explanation for $I_{threshold}$ in view of the DP theory.

Bibliography

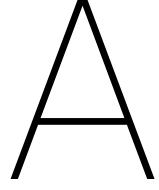
- [1] Lanny D Schmidt. *The engineering of chemical reactions*. Oxford University Press New York, 2005.
- [2] André B de Haan and Hans Bosch. *Industrial separation processes: Fundamentals*. Walter de Gruyter, 2013.
- [3] European Chemical Engineering Council. Facts & figures of the European chemical industry, 2018. Available: cefic.org/app/uploads/2018/12/Cefic_FactsAnd_Figures_2018_Industrial_BROCHURE_TRADE.pdf [Accessed: 19 - Aug - 2019].
- [4] John Conti, Paul Holtberg, Jim Diefenderfer, Angelina LaRose, James T Turnure, and Lynn Westfall. International energy outlook 2016 with projections to 2040. Technical report, USDOE Energy Information Administration (EIA), Washington, DC United States, 2016.
- [5] Wenjing Li, Aziza Ikni, Philippe Scouflaire, Xiaoxuan Shi, Nouha El Hassan, Pascale Gemeiner, Jean-Michel Gillet, and Anne Spasojevic-de Bire. Non-photochemical laser-induced nucleation of sulfathiazole in a water/ethanol mixture. *Crystal Growth & Design*, 16(5):2514–2526, 2016.
- [6] Bertrand Clair, Aziza Ikni, Wenjing Li, Philippe Scouflaire, Vincent Quemener, and Anne Spasojević-de Biré. A new experimental setup for high-throughput controlled non-photochemical laser-induced nucleation: application to glycine crystallization. *Journal of Applied Crystallography*, 47(4):1252–1260, 2014.
- [7] Marco Nardone and Victor G Karpov. A phenomenological theory of nonphotochemical laser induced nucleation. *Physical Chemistry Chemical Physics*, 14(39):13601–13611, 2012.
- [8] Stéphane Veessler, Kenji Furuta, Hiroaki Horiuchi, Hiroshi Hiratsuka, Natalie Ferté, and Tetsuo Okutsu. Crystals from light: photochemically induced nucleation of hen egg-white lysozyme. *Crystal growth & design*, 6(7):1631–1635, 2006.
- [9] Andrew J Alexander and Philip J Camp. Non-photochemical laser-induced nucleation. *The Journal of chemical physics*, 150(4):040901, 2019.
- [10] Pablo G Debenedetti. *Metastable liquids: concepts and principles*. Princeton University Press, 1996.
- [11] Farid Abraham. *Homogeneous nucleation theory: the pretransition theory of vapor condensation*, volume 1. Elsevier, 2012.
- [12] M Scott Shell. *Thermodynamics and statistical mechanics: an integrated approach*. Cambridge University Press, 2015.
- [13] Deniz Erdemir, Alfred Y Lee, and Allan S Myerson. Nucleation of crystals from solution: classical and two-step models. *Accounts of chemical research*, 42(5):621–629, 2009.
- [14] G Job and F Herrmann. Chemical potential—a quantity in search of recognition. *European journal of physics*, 27(2):353, 2006.
- [15] Nasrin Mirsaleh-Kohan, Andrew Fischer, Bernard Graves, Mehdi Bolorizadeh, Dilip Kondepudi, and Robert N Compton. Laser shock wave induced crystallization. *Crystal Growth & Design*, 17(2):576–581, 2017.
- [16] Jihan Zhou, Yongsoo Yang, Yao Yang, Dennis S Kim, Andrew Yuan, Xuezheng Tian, Colin Ophus, Fan Sun, Andreas K Schmid, Michael Nathanson, et al. Observing crystal nucleation in four dimensions using atomic electron tomography. *Nature*, 570(7762):500, 2019.

- [17] BA Garetz, JE Aber, NL Goddard, RG Young, and AS Myerson. Nonphotochemical, polarization-dependent, laser-induced nucleation in supersaturated aqueous urea solutions. *Physical review letters*, 77(16):3475, 1996.
- [18] Julien Zaccaro, Jelena Matic, Allan S Myerson, and Bruce A Garetz. Nonphotochemical, laser-induced nucleation of supersaturated aqueous glycine produces unexpected γ -polymorph. *Crystal Growth & Design*, 1(1):5–8, 2001.
- [19] Maria J Vesga, David McKechnie, Paul A Mulheran, Karen Johnston, and Jan Sefcik. Conundrum of γ glycine nucleation revisited: to stir or not to stir? *CrystEngComm*, 21(13):2234–2243, 2019.
- [20] Shubo Wang, Sumei Wang, Lan Jiang, Mengmeng Wang, Yuyin Wei, Jiabin Sun, Shenghua Zhan, Xin Li, and Liangti Qu. Polymorph-controlled crystallization of acetaminophen through femtosecond laser irradiation. *Crystal Growth & Design*, 2019.
- [21] Tasfia Tasnim, Audrey Goh, Omar Gowayed, Chunhua T Hu, Tzu-Yi Chen, Janice E Aber, and Bruce A Garetz. Dendritic growth of glycine from nonphotochemical laser-induced nucleation of supersaturated aqueous solutions in agarose gels. *Crystal Growth & Design*, 18(10):5927–5933, 2018.
- [22] Yao Liu, Martin R Ward, and Andrew J Alexander. Polarization independence of laser-induced nucleation in supersaturated aqueous urea solutions. *Physical Chemistry Chemical Physics*, 19(5):3464–3467, 2017.
- [23] Tianyi Hua, Omar Gowayed, Danielle Grey-Stewart, Bruce A Garetz, and Ryan L Hartman. Microfluidic laser-induced nucleation of supersaturated aqueous kcl solutions. *Crystal Growth & Design*, 2019.
- [24] Matthias Lenzner, Jörg Krüger, S Sartania, Z Cheng, Ch Spielmann, G Mourou, Wolfgang Kautek, and Ferenc Krausz. Femtosecond optical breakdown in dielectrics. *Physical review letters*, 80(18):4076, 1998.
- [25] Matthew S Brown and Craig B Arnold. Fundamentals of laser-material interaction and application to multiscale surface modification. In *Laser precision microfabrication*, pages 91–120. Springer, 2010.
- [26] Finlay Walton and Klaas Wynne. Control over phase separation and nucleation using a laser-tweezing potential. *Nature chemistry*, 10(5):506, 2018.
- [27] Max Born and Emil Wolf. *Principles of optics: electromagnetic theory of propagation, interference and diffraction of light*. Elsevier, 2013.
- [28] Janice E Aber, Stephen Arnold, Bruce A Garetz, and Allan S Myerson. Strong dc electric field applied to supersaturated aqueous glycine solution induces nucleation of the γ polymorph. *Physical review letters*, 94(14):145503, 2005.
- [29] David J Griffiths. *Introduction to electrodynamics*. Prentice Hall, 2005.
- [30] Donald G Truhlar and Bruce C Garrett. Variational transition state theory. *Annual Review of Physical Chemistry*, 35(1):159–189, 1984.
- [31] Jelena Matic, Xiaoying Sun, Bruce A Garetz, and Allan S Myerson. Intensity, wavelength, and polarization dependence of nonphotochemical laser-induced nucleation in supersaturated aqueous urea solutions. *Crystal growth & design*, 5(4):1565–1567, 2005.
- [32] Rahul Malik, Damian Burch, Martin Bazant, and Gerbrand Ceder. Particle size dependence of the ionic diffusivity. *Nano letters*, 10(10):4123–4127, 2010.
- [33] VM Yurov, SA Guchenko, and MS Gyngazova. Effect of an electric field on nucleation and growth of crystals. In *IOP Conference Series: Materials Science and Engineering*, volume 110, page 012019. IOP Publishing, 2016.
- [34] Robert C Weast, Melvin J Astle, William H Beyer, et al. *CRC handbook of chemistry and physics*, volume 69. CRC press Boca Raton, FL, 1988.
- [35] Martin R Ward, Iain Ballingall, Matthew L Costen, Kenneth G McKendrick, and Andrew J Alexander. Nanosecond pulse width dependence of nonphotochemical laser-induced nucleation of potassium chloride. *Chemical Physics Letters*, 481(1-3):25–28, 2009.

- [36] Kazuhiko Nakamura, Yoichiro Hosokawa, and Hiroshi Masuhara. Anthracene crystallization induced by single-shot femtosecond laser irradiation: Experimental evidence for the important role of bubbles. *Crystal growth & design*, 7(5):885–889, 2007.
- [37] MN Afsar, John Chamberlain, and George W Chantry. High-precision dielectric measurements on liquids and solids at millimeter and submillimeter wavelengths. *IEEE Transactions on Instrumentation and Measurement*, (4):290–294, 1976.
- [38] JY Jo, DJ Kim, YS Kim, S-B Choe, TK Song, J-G Yoon, and TW Noh. Polarization switching dynamics governed by the thermodynamic nucleation process in ultrathin ferroelectric films. *Physical review letters*, 97(24):247602, 2006.
- [39] Andrew J Alexander and Philip J Camp. Single pulse, single crystal laser-induced nucleation of potassium chloride. *Crystal Growth and Design*, 9(2):958–963, 2008.
- [40] Brandon C Knott, Jerry L LaRue, Alec M Wodtke, Michael F Doherty, and Baron Peters. Communication: Bubbles, crystals, and laser-induced nucleation, 2011.
- [41] Xiaoying Sun, Bruce A Garetz, and Allan S Myerson. Supersaturation and polarization dependence of polymorph control in the nonphotochemical laser-induced nucleation (nplin) of aqueous glycine solutions. *Crystal growth & design*, 6(3):684–689, 2006.
- [42] Martin R Ward, Stephanie McHugh, and Andrew J Alexander. Non-photochemical laser-induced nucleation of supercooled glacial acetic acid. *Physical Chemistry Chemical Physics*, 14(1):90–93, 2012.
- [43] Martin R Ward, Alasdair M Mackenzie, and Andrew J Alexander. Role of impurity nanoparticles in laser-induced nucleation of ammonium chloride. *Crystal Growth & Design*, 16(12):6790–6796, 2016.
- [44] Rohit Kacker, Sanjana Dhingra, Daniel Irimia, Murali Krishna Ghatkesar, Andrzej Stankiewicz, Herman JM Kramer, and Huseyin Burak Eral. Multiparameter investigation of laser-induced nucleation of supersaturated aqueous kcl solutions. *Crystal Growth & Design*, 18(1):312–317, 2017.
- [45] Nadeem Javid, Thomas Kendall, Iain S Burns, and Jan Sefcik. Filtration suppresses laser-induced nucleation of glycine in aqueous solutions. *Crystal Growth & Design*, 16(8):4196–4202, 2016.
- [46] David R Lide. *CRC handbook of chemistry and physics*, volume 85. CRC press, 2004.
- [47] Chao Sun, Edip Can, Rory Dijkink, Detlef Lohse, and Andrea Prosperetti. Growth and collapse of a vapour bubble in a microtube: the role of thermal effects. *Journal of fluid mechanics*, 632:5–16, 2009.
- [48] Qinggong Wang, Wei Yao, Xiaojun Quan, and Ping Cheng. Validation of a dynamic model for vapor bubble growth and collapse under microgravity conditions. *International Communications in Heat and Mass Transfer*, 95:63–73, 2018.
- [49] Niklas Hidman, Gaetano Sardina, Dario Maggiolo, Henrik Ström, and Srdjan Sasic. Laser-induced vapour bubble as a means for crystal nucleation in supersaturated solutions—formulation of a numerical framework. *Experimental and Computational Multiphase Flow*, 1(4):242–254, 2019.
- [50] Anamaria Soare, Rory Dijkink, Marcos Rodriguez Pascual, Chao Sun, Peter W Cains, Detlef Lohse, Andrzej I Stankiewicz, and Herman JM Kramer. Crystal nucleation by laser-induced cavitation. *Crystal growth & design*, 11(6):2311–2316, 2011.
- [51] Takayuki Uwada, Sho Fujii, Teruki Sugiyama, Anwar Usman, Atsushi Miura, Hiroshi Masuhara, Katsuhiko Kanaizuka, and Masa-aki Haga. Glycine crystallization in solution by cw laser-induced microbubble on gold thin film surface. *ACS applied materials & interfaces*, 4(3):1158–1163, 2012.
- [52] Mohammad Taghi Shervani-Tabar. Computer study of a cavity bubble near a rigid boundary, a free surface, and a compliant wall. 1995.
- [53] Julien O Sindt, Andrew J Alexander, and Philip J Camp. Effects of nanoparticle heating on the structure of a concentrated aqueous salt solution. *The Journal of chemical physics*, 147(21):214506, 2017.

- [54] Thomas P van Waas. Molecular dynamics simulations of aggregation cluster formation by cavitation bubble formation. Bachelor thesis, Delft University of Technology, 2019. In preparation.
- [55] Anamaria Soare. Technologies for optimisation and control of nucleation and growth for new generations of industrial crystallizers. 2014.
- [56] Tibor Juhasz, George A Kastis, Carlos Suárez, Zsolt Bor, and Walter E Bron. Time-resolved observations of shock waves and cavitation bubbles generated by femtosecond laser pulses in corneal tissue and water. *Lasers in Surgery and Medicine: The Official Journal of the American Society for Laser Medicine and Surgery*, 19(1):23–31, 1996.
- [57] Y Tomita and A Shima. Mechanisms of impulsive pressure generation and damage pit formation by bubble collapse. *Journal of Fluid Mechanics*, 169:535–564, 1986.
- [58] Kazuhiko Nakamura, Yosuke Sora, Hiroshi Y Yoshikawa, Yoichiroh Hosokawa, Ryota Murai, Hiroaki Adachi, Yusuke Mori, Takatomo Sasaki, and Hiroshi Masuhara. Femtosecond laser-induced crystallization of protein in gel medium. *Applied surface science*, 253(15):6425–6429, 2007.
- [59] Jasmine A Jacob, Sébastien Sorgues, Alexandre Dazzi, Mehran Mostafavi, and Jacqueline Belloni. Homogeneous nucleation-growth dynamics induced by single laser pulse in supersaturated solutions. *Crystal Growth & Design*, 12(12):5980–5985, 2012.
- [60] Yoshiyuki Tagawa, Shota Yamamoto, Keisuke Hayasaka, and Masaharu Kameda. On pressure impulse of a laser-induced underwater shock wave. *Journal of Fluid Mechanics*, 808:5–18, 2016.
- [61] Alfred Vogel, Kester Nahen, Dirk Theisen, and Joachim Noack. Plasma formation in water by picosecond and nanosecond nd: Yag laser pulses. i. optical breakdown at threshold and superthreshold irradiance. *IEEE Journal of Selected Topics in Quantum Electronics*, 2(4):847–860, 1996.
- [62] Alfred Vogel, Joachim Noack, G Hüttman, and GJAPB Paltauf. Mechanisms of femtosecond laser nanosurgery of cells and tissues. *Applied Physics B*, 81(8):1015–1047, 2005.
- [63] The Engineering Toolbox. Density of aqueous solutions of inorganic potassium salts. Available: https://www.engineeringtoolbox.com/density-aqueous-solution-inorganic-potassium-salt-concentration-d_1956.html. [Accessed: 19 - Aug - 2019].
- [64] Python Software Foundation. Python Version 3.7.0. [Computer software], Dover, Delaware, 2019.
- [65] PCO Imaging. PCO Dimax 4. [Computer software], Kelheim, Germany, 2019.
- [66] MathWorks Inc. MATLAB Version 9.6.0 (R2019a), 2019. [Computer software], Natick, Massachusetts, 2019.
- [67] Stanford Research Systems. MODEL DG535 Digital Delay / Pulse Generator, 2017. Available: <https://www.thinksrs.com/downloads/pdfs/manuals/DG535m.pdf>. [Accessed: 16 - Aug - 2019].
- [68] Continuum@. PowerLite DLS 8000 Series Datasheet, 2017. Available: <https://www.photonicsolutions.co.uk/upfiles/PowerliteDLS8000SeriesDatasheetLG07Dec17.pdf>. [Accessed: 16 - Aug - 2019].
- [69] Ra’ef Mikhail. Testing the limits: Ldt considerations when selecting laser optics. *Optik & Photonik*, 7(2):53–55, 2012.
- [70] PCO Imaging. PCO Dimax S4 product data sheet, 2009. Available: https://www.pco.de/fileadmin/user_upload/pcoproduct_sheets/pco.dimax_s_data_sheet.pdf. [Accessed: 16 - Aug - 2019].
- [71] Mikrotron GmbH. Eosens 3cl camera manual, 2010. Available: https://mikrotron.de/fileadmin/content/download/overview-manuals-for-download/EoSens_3CL_MC3010-11_man_e.pdf. [Accessed: 16 - Aug - 2019].

- [72] Christos Danakis, Mostafa Afgani, Gordon Povey, Ian Underwood, and Harald Haas. Using a cmos camera sensor for visible light communication. In *2012 IEEE Globecom Workshops*, pages 1244–1248. IEEE, 2012.
- [73] Curtis A Corum, Kevin M Connolly, and Edward J Bawolek. Dark frame subtraction, August 8 2000. US Patent 6,101,287.
- [74] RS Components LTD. Rs pro white acrylic sealant paste tube. Available: <https://uk.rs-online.com/web/p/acrylic-sealants/0557146/>. [Accessed: 18 - Aug - 2019].
- [75] Allan Myerson. *Handbook of industrial crystallization*. Butterworth-Heinemann, 2002.
- [76] Shufan Cai. The mechanism of cavitation bubble in non-photochemical laser induced nucleation. Masters thesis, Delft University of Technology, The Netherlands, 2019.
- [77] WaveMetrics, Inc. An Airy Disk PSF, 2012. Available: <https://www.wavemetrics.com/forum/general/airy-disk-psf>. [Accessed: 17 - Aug - 2019].
- [78] Vision Research. Phantom v2512 Datasheet, 2018. Available: <https://www.phantomhighspeed.com/products/cameras/ultrahighspeed/v2512> [Accessed: 18 - Aug - 2019].
- [79] Daniel Selzer, Burkard Spiegel, and Matthias Kind. A generic polycarbonate based microfluidic tool to study crystal nucleation in microdroplets. *Journal of Crystallization Process and Technology*, 8(1):1–17, 2017.
- [80] I. Hughes and T. Hase. *Measurements and their uncertainties: A practical guide to modern error analysis*. Oxford University Press, 2010.
- [81] Frederik M Dekking, Cornelis Kraaikamp, Hendrik P Lopuhaä, and Ludolf Erwin Meester. *A Modern Introduction to Probability and Statistics: Understanding why and how*. Springer Science & Business Media, 2005.



Uncertainties

The uncertainty $u(F(a_1, a_2, a_3, \dots, a_n))$ of an arbitrary function $F(a_1, a_2, a_3, \dots, a_n)$ of variables $a_1, a_2, a_3, \dots, a_n$ is given by [80]:

$$u(F(a_1, a_2, \dots, a_n)) = \sqrt{\sum_{i=1}^n \left(\frac{\partial F(a_1, a_2, \dots, a_n)}{\partial a_i} u(a_i) \right)^2}. \quad (\text{A.1})$$

In this report, Equation A.1 has been used for propagation of uncertainties. Specifically, all data is displayed with 95% confidence intervals. According to the Central Limit Theorem, the probability that the mean \bar{x} of a Gaussian variable x falls within 1.96 times the confidence interval with standard uncertainty $u(x)$ for N independent data points is given by

$$P\left(-1.96 \leq \frac{\bar{x} - \mu_x}{\sigma_x / \sqrt{N}} \leq 1.96\right) = 0.95, \quad (\text{A.2})$$

where σ_x is the standard deviation of x , μ_x is the mean of x , and the standard uncertainty $u(x)$ is related to the standard deviation as [81]:

$$u(x) = \frac{\sigma_x}{\sqrt{N}}. \quad (\text{A.3})$$

Equation A.2 has been used for determining confidence intervals for variables based on multiple data points. For least squares fitting, the weight attributed to each data point with uncertainty $u(x)$ is given as [80]:

$$w(x) = \frac{1}{\sigma_x^2}. \quad (\text{A.4})$$

The standard deviation of a sample set of size N was calculated as

$$\sigma_x = \sqrt{\frac{\sum_{i=1}^N (x_i - \mu_x)^2}{n-1}}, \quad (\text{A.5})$$

and the standard uncertainty from the sample set was calculated using Equation A.3.